Published in final edited form as:
Nature. 2021 September ; 597(7874): 97–102. doi:10.1038/s41586-021-03807-6.

SARS-CoV-2 RBD antibodies that maximize breadth and resistance to escape

A full list of authors and affiliations appears at the end of the article.

Abstract

An ideal anti-SARS-CoV-2 antibody would resist viral escape[1–3], have activity against diverse SARS-related coronaviruses (sarbecoviruses)[4–7], and be highly protective through viral neutralization[8–11] and effector functions[12,13]. Understanding how these properties relate to each other and vary across epitopes would aid development of antibody therapeutics and guide vaccine design. Here, we comprehensively characterize escape, breadth, and potency across a panel of SARS-CoV-2 antibodies targeting the receptor-binding domain (RBD). Despite a tradeoff between *in vitro* neutralization potency and breadth of sarbecovirus binding, we identify neutralizing antibodies with exceptional sarbecovirus breadth and a corresponding resistance to SARS-CoV-2 escape. One of these antibodies, S2H97, binds with high affinity across all sarbecovirus clades to a previously undescribed cryptic epitope and prophylactically protects hamsters from viral challenge. Antibodies targeting the ACE2 receptor binding motif (RBM) typically have poor breadth and are readily escaped by mutations despite high neutralization potency. Nevertheless, we characterize one potent RBM antibody (S2E12[8]) with breadth across sarbecoviruses related to SARS-CoV-2 and a high barrier to viral escape. These data highlight principles underlying variation in escape, breadth, and potency among antibodies targeting the RBD, and identify

---

[†]Correspondence and requests for materials should be addressed to Davide Corti (dcorti@vir.bio), Jesse D. Bloom (jbloom@fredhutch.org), and Gyorgy Snell (gsnell@vir.bio).
[*]These authors contributed equally

AUTHOR CONTRIBUTIONS

Conceived research and designed study: TNS, NC, HWV, DC, JDB, GS. Antibody discovery: FZ, DP, MB, RM, ADM, EC, MSP, DC. Expression and purification of proteins: NC, PH, GL, NS, JEB, ACW, KC, SJ, MM. Antibody functional experiments: YJP, ZL, FZ, DP, MB, RM, JEB, MAT, ACW, JAW, ADM, LER, JZ, MMR, HK, JD, HT, JB, CSF, MPH, MA, ED, SS, CHD, LP, FB, FAL, SPJW. Deep mutational scanning experiments and analysis: TNS, AA, AJG, ASD. Hamster model: RA, SCF, FB, JN. Bioinformatics analysis: JDI, AT. Structure determination: NC, YJP, PH, JEB, TIC, JCN, DV, GS. Molecular dynamics simulation and analysis: WGG, IZ, JDC. Supervision: MSP, JDC, CMH, SPJW, DV, DC, JDB, GS. Wrote the initial draft: TNS, NC, DC, JDB, GS. Edited the final version: all authors.

DECLARATION OF INTERESTS

NC, FZ, DP, MB, PH, RM, JAW, ADM, LER, JZ, MMR, HK, JD, HT, JB, CSF, MPH, JDI, GL, MA, NS, KC, SJ, MM, ED, EC, CHD, LP, FB, AT, FAL, MSP, CMH, HWV, DC and GS are or were employees of Vir Biotechnology and may hold shares in Vir Biotechnology. DC is currently listed as an inventor on multiple patent applications, which disclose the subject matter described in this manuscript. After the submission of the initial version of this study, JDB began consulting for Moderna on viral evolution and epidemiology. JDB has the potential to receive a share of IP revenue as an inventor on a Fred Hutchinson Cancer Research Center-optioned technology/patent (application WO2020006494) related to deep mutational scanning of viral proteins. HWV is a founder of PierianDx and Casma Therapeutics. Neither company provided funding for this work nor is performing related work. JCN, TIC, and DV are consultants for Vir Biotechnology Inc. The Veesler laboratory has received a sponsored research agreement from Vir Biotechnology Inc. JDC is a current member of the Scientific Advisory Boards of OpenEye Scientific Software, Interline Therapeutics, and Redesign Science. The Chodera laboratory receives or has received funding from the National Institute of Health, the National Science Foundation, the Parker Institute for Cancer Immunotherapy, Relay Therapeutics, Entasis Therapeutics, Silicon Therapeutics, EMD Serono (Merck KGaA), AstraZeneca, Vir Biotechnology, XtalPi, Interline Therapeutics, and the Molecular Sciences Software Institute, the Starr Cancer Consortium, the Open Force Field Consortium, Cycle for Survival, a Louis V. Gerstner Young Investigator Award, and the Sloan Kettering Institute. A complete funding history for the Chodera lab can be found at http://choderalab.org/funding. The other authors declare no competing interests.

epitopes and features to prioritize for therapeutic development against the current and potential future pandemics.

The most potently neutralizing antibodies to SARS-CoV-2—including those in clinical use[14] and dominant in polyclonal sera[15,16]—target the spike receptor-binding domain (RBD). Mutations in the RBD that reduce binding by antibodies have emerged among SARS-CoV-2 variants[17–21], highlighting the need for antibodies and vaccines that are robust to viral escape. We have previously described an antibody, S309[4], that exhibits potent effector functions and neutralizes all current SARS-CoV-2 variants[22,23] and the divergent sarbecovirus SARS-CoV-1. S309 forms the basis for an antibody therapy (VIR-7831, recently renamed sotrovimab) that has received Emergency Use Authorization for treatment of COVID-19[24]. Longer term, antibodies with broad activity across SARS-related coronaviruses (sarbecoviruses) would be useful to combat potential future spillovers[6]. These efforts would be aided by a systematic understanding of the relationships among antibody epitope, resistance to viral escape, and breadth of sarbecovirus cross-reactivity. Here we address this question by comprehensively characterizing a diverse panel of antibodies, including S309, using deep mutational scanning, pan-sarbecovirus binding assays, *in vitro* selection of viral escape, and biochemical and structural analyses.

Potency, escapability, and breadth in a panel of RBD antibodies

We identified a panel of anti-SARS-CoV-2 antibodies with distinct properties (Fig. 1a, Extended Data Table 1), including six antibodies newly described in this study. These antibodies bind different epitopes within the receptor-binding motif (RBM) and the non-RBM “core” of the RBD. The antibody panel spans a range of neutralization potencies and binding affinities (Fig. 1a, Extended Data Fig. 1a–c).

We used deep mutational scanning to map how all amino-acid mutations in the SARS-CoV-2 RBD affect binding by each antibody[3] (Fig. 1b,c and Extended Data Fig. 2). Some antibodies have narrowly focused functional epitopes (the set of residues where mutations abolish binding[25]), with binding-escape mutations at just a few key residues (e.g., S309, S2D106), while other antibodies have wider functional epitopes (e.g., S2H13; tabulations at right in Fig. 1b,c). We previously measured how all RBD mutations affect folded RBD expression and ACE2 binding affinity[26] (letter colors in Fig. 1b,c). We used the combined measures of how mutations affect antibody binding and RBD function to compute the “escapability” of each antibody, which reflects the extent to which mutations that escape antibody binding are functionally tolerated (Fig. 1b,c and Extended Data Fig. 3a,b). We also investigated the sensitivity of each antibody to mutations among SARS-CoV-2 sequences reported in GISAID (heatmap below logoplots in Fig. 1b,c; Extended Data Fig. 3c), and found that some antibodies are more affected by natural SARS-CoV-2 mutations than others, including mutations found in SARS-CoV-2 variants of concern (Extended Data Fig. 1d)[27–29].

We next extended our deep mutational scanning platform to measure binding of each antibody to a pan-sarbecovirus panel of 45 RBDs (Fig. 1d and Extended Data Fig. 4a–f). The four antibodies that bind the core RBD exhibit cross-reactive binding to RBDs from

SARS-CoV-1 and related ACE2-utilizing bat sarbecoviruses, and from sarbecoviruses in Europe and Africa. Antibodies S304 and S2H97 also bind RBDs of the most divergent clade from Asia that have an average 64% amino acid identity with SARS-CoV-2. S2H97 exhibits notably tight binding to all RBDs tested (Fig. 1d and Extended Data Fig. 4f), making it the broadest pan-sarbecovirus RBD antibody described to date. Antibodies that bind epitopes within the RBM exhibit more limited cross-reactivity, typically binding only SARS-CoV-2 and the closely related GD-Pangolin-CoV RBD. S2E12 stands out among the RBM antibodies we evaluated as it also binds the RaTG13 and GX-Pangolin-CoV RBDs, showing that even within the evolutionarily plastic RBM[19,26] there are epitopes that enable greater breadth than others.

The pan-sarbecovirus S2H97 antibody

To understand the structural basis for cross-reactive sarbecovirus binding, we determined the structures of S2H97 Fab (X-ray crystallography, 2.65 Å resolution), S2X35 Fab (X-ray crystallography, 1.83 Å resolution), and S2E12 Fab (X-ray crystallography, 2.95 Å resolution) bound to SARS-CoV-2 RBD (Fig. 2a and Extended Data Table 2). This panel of cross-reactive antibodies emphasizes the core RBD as a general target of broad antibody binding due to its conservation among sarbecoviruses, reflected in the diverse core RBD surfaces targeted by the broadest of these antibodies (Fig. 2a and Extended Data Fig. 5a–f).

The exceptionally cross-reactive S2H97 antibody targets a previously undescribed cryptic antigenic site, which we designated site V (Fig. 2a,b). S2H97 binding is facilitated by packing of the heavy chain CDR3 into an RBD crevice at the center of the epitope, together with polar contacts with all three heavy chain CDRs and the light chain CDR2 (Extended Data Fig. 5f). Molecular dynamics simulation of the S2H97 Fab:RBD complex highlights the durability of many of these interactions (Fig. 2b). The surface bound by S2H97 is constrained by the deleterious effects of mutations on folded RBD expression (Fig. 2b)[26], and this constraint is likely enhanced by quaternary packing with the NTD in the closed spike trimer (Extended Data Fig. 6a). Consistent with the conservation of the S2H97 epitope, S2H97 neutralizes diverse sarbecoviruses (Fig. 2c and Extended Data Fig. 4g) and SARS-CoV-2 variants (Fig. 2d).

To understand the evolution of S2H97 breadth, we measured breadth of binding by its germline form, S2H97$_{GL}$, in which we reverted the 13 somatic mutations (Extended Data Fig. 4h,i). S2H97$_{GL}$ bound all tested sarbecovirus RBDs and exhibited particularly high affinity for SARS-CoV-2-related RBDs. Somatic mutations enhanced affinity across all sarbecoviruses by two orders of magnitude. This general increase in affinity together with the absence of non-conservative amino acid replacements among paratope residues suggests that framework mutations may contribute to a general improvement in S2H97 binding affinity.

To characterize the mechanism of S2H97 neutralization, we determined a cryoEM structure of S2H97 bound to SARS-CoV-2 S (Extended Data Fig. 5i–l and Extended Data Table 3). S2H97 binding requires extensive opening of the RBD to unmask its cognate epitope (Extended Data Fig. 6b), even more than is required to access the cryptic antigenic site II[15].

Like other antibodies that only bind the open RBD[30,31], S2H97 induces rapid and premature refolding of spike into the post-fusion state (Fig. 2e), promotes S1 shedding of cell-surface-expressed spike (Extended Data Fig. 6c), and induces a low level of syncytia formation among spike-expressing cells (Extended Data Fig. 6d). S2H97 does not interfere with ACE2 binding (Extended Data Fig. 6e). Like other non-ACE2-competitive antibodies[31,32], S2H97 neutralization is attenuated in cells that over-express ACE2 (Extended Data Fig. 6f). Consistent with its ability to neutralize spike-mediated viral entry, S2H97 inhibits spike-mediated cell-cell fusion (Extended Data Fig. 6g). Taken together, these experiments suggest that the S2H97 mechanism of neutralization involves receptor-independent conversion of S to the post-fusion state[30], thereby inhibiting ACE2-mediated cell entry.

Next, we determined the prophylactic efficacy of S2H97 *in vivo* using a Syrian hamster model of infection. We administered hamsters with S2H97 at 25 mg/kg two days prior to intranasal challenge with SARS-CoV-2 and assessed viral RNA load and infectious viral titers in the lungs four days post-infection. S2H97 prophylaxis reduced RNA copies by >10,000-fold relative to control in the four animals that had detectable circulating antibody levels at the time of challenge and reduced infectious viral titers to the lower detection limit in these animals (Fig. 2f). The two animals without a reduction in viral load had circulating S2H97 levels below the limit of quantification (50 ng/ml) at the time of viral challenge (Extended Data Fig. 6h), which may reflect a failure in the intraperitoneal administration procedure. Therefore, S2H97 demonstrates that antibodies to the newly identified antigenic site V can be protective *in vivo*.

Last, we performed serum blockade of binding experiments[15], demonstrating that antibodies competing with S2H97 binding are rare in infection- and vaccine-elicited sera (Fig. 2g). This sub-dominance of antigenic site V may be explained by the inaccessibility of the epitope as illustrated in the cryoEM structure. However, the protective nature and exceptional breadth of S2H97 suggests that updated immunogen designs, such as those based on the RBD[33–35], could unmask antigenic site V to better elicit S2H97-like antibodies.

Variation in breadth and escapability among RBM epitopes

Our survey reveals variation in the escapability and breadth of antibodies that target the RBM (Fig. 1c,d), which is immunodominant (Fig. 2g) but variable over sarbecovirus and SARS-CoV-2 evolution. We performed *in vitro* selection experiments to identify spike-expressing VSV mutants that emerge in the presence of each of seven monoclonal antibodies (Fig. 3a and Extended Data Fig. 7a,b) to further understand escape from these antibodies.

Many RBM antibodies such as S2X58 and S2D106 select mutations present in SARS-CoV-2 variants of concern (e.g., L452R and E484K)[27–29]. In contrast, S2E12 selects viral mutants at sites that do not exhibit substantial variation among circulating SARS-CoV-2, and S2E12 correspondingly neutralizes a diverse panel of SARS-CoV-2 variants (Fig. 3b)[17]. S2E12 is also unique in its breadth among RBM antibodies (Fig. 1d), neutralizing VSV pseudotyped with each of the four SARS-CoV-2 clade sarbecovirus spikes (Fig. 3c and Extended Data Fig. 4j). As with S2H97, somatic mutations in S2E12 enhanced affinity across sarbecoviruses, though the increase in affinity was more modest than for S2H97 (Extended Data Fig. 4k,l).

Conservation of the S2E12 epitope among SARS-CoV-2 variants could reflect the relative rarity of S2E12-like antibodies in polyclonal sera leading to little antigenic pressure at these sites (Fig. 2g), together with functional constraint in the S2E12 epitope (escapability being the lowest for S2E12 and S2H97 among the 12 antibodies evaluated). Indeed, the strong antibody-escape mutations that emerged in S2E12 viral escape selections decrease ACE2 binding affinity (Fig. 3a)[26] and reduce replicative fitness in a bulk competition experiment between spike-expressing VSV variants passaged in the absence of antibody (Fig. 3d).

To understand the structural basis for the unique breadth and robustness of S2E12 to escape, we compared its structure to that of S2D106 Fab (cryoEM, 4.0 Å resolution local refinement) bound to SARS-CoV-2 RBD (Fig. 3e,f, Extended Data Fig. 5g,h,m–p and Extended Data Tables 2, 3). We also integrated evolutionary, functional, and structural details for the sites in each antibody's structural footprint (Fig. 3g,h). S2E12 and S2D106 bind the receptor-binding ridge, with 8 residues shared between their footprints. S2E12 binding is oriented toward extensive packing of the ACE2-contact residue $F486_{RBD}$ within a cavity lined by aromatic residues at the antibody light/heavy-chain interface (Fig. 3e and Extended Data Fig. 5g), as was seen with the homologous antibody COV2-2196[36]. Sites within the S2E12 footprint that exhibit less functional constraint (e.g., E484, S477) are located at the periphery of the interface, explaining the robustness of S2E12 toward SARS-CoV-2 variants (Fig. 3b,g). This structural interface also explains the breadth of S2E12 toward RaTG13 and GX-Pangolin-CoV (Fig. 1d), as the F486L mutation present in these sarbecoviruses retains the central hydrophobic packing.

In contrast to S2E12, S2D106 binding is centered on residue $E484_{RBD}$ which may form a salt bridge with $R96_{LC}$, in addition to nonpolar contacts between $F490_{RBD}$ and residues in the heavy chain CDR2 (Fig. 3f and Extended Data Fig. 5h). Although the long heavy chain CDR3 packs intimately across the surface of the RBD, there are no crucial CDRH3:RBD contacts that are sensitive to mutation. S2D106 escape is therefore highly focused on E484 and F490, which are functionally tolerant and exhibit variation among SARS-CoV-2 sequences (Fig. 3h). This comparison between S2E12 and S2D106 highlights how small differences in the RBD:antibody interface impact the breadth and robustness of each antibody to viral escape.

The landscape of RBD epitopes

Last, we examined how escapability, breadth, and neutralization potency relate to one another and to RBD epitope. We used our binding-escape maps (Fig. 1b,c), together with comparable maps published for other RBD antibodies[3,20,21,36,37], to project antibodies into a two-dimensional space based on similarities in sites of binding-escape mutations (Fig. 4a).

We annotated our projection of epitope space by antibody properties such as *in vitro* neutralization potency, breadth, and escapability (Fig. 4b–d and Extended Data Fig. 7c,d). The most potently neutralizing antibodies (e.g., S2E12, S2D106) bind epitopes in the

RBM, while antibodies targeting the core RBD are less potently neutralizing (Fig. 4b). It is important to note that RBD antibodies can protect *in vivo* through other mechanisms beyond neutralization[12,13,22]. Antibodies with broad sarbecovirus binding target the core RBD (Fig. 4c). Our panel therefore extends prior observations[4,5,32,38] to highlight a general tradeoff between sarbecovirus breadth and potency of SARS-CoV-2 neutralization (Fig. 4e). Nonetheless, some cross-reactive antibodies exhibit intermediate *in vitro* neutralization potency (e.g., S309, S2X259[37]), and the highly potent RBM-directed antibody S2E12 exhibits modest breadth, highlighting the existence of antibodies that balance neutralization potency and breadth.

The size of an antibody's functional epitope (Fig. 1b,c) is not strongly influenced by the epitope's structural location (Extended Data Fig. 7c)—instead, narrower functional epitopes are associated with higher Fab:RBD binding affinity (Fig. 4f). However, an antibody's escapability, which integrates how escape mutations affect RBD folding and ACE2 affinity, is influenced by variation in these functional constraints across the RBD structure. For example, antibodies that cluster with S2E12 exhibit lower escapability (Extended Data Fig. 7c) and frequency of natural SARS-CoV-2 escape mutants (Fig. 4d). As highlighted in our detailed descriptions of S2E12 and S2H97 above, a modest degree of breadth of sarbecovirus binding is associated with a greatly reduced frequency of escape mutations among circulating SARS-CoV-2 variants (Fig. 4g).

Principles for optimizing antibody and vaccine development

Ongoing SARS-CoV-2 evolution[19,27–29], long-term antigenic evolution of other human coronaviruses[39,40], and the spillover potential of diverse sarbecovirus lineages[6,7] indicate the importance of developing antibodies and vaccines that are robust to viral evolution. In this work, we identify antibody and epitope features which can guide this process. Although *in vitro* neutralization potency is often prioritized for lead selection, our results suggest this will bias antibodies toward RBM epitopes, many of which are poorly conserved in the short-term evolution of SARS-CoV-2[19] and the long-term evolution of sarbecoviruses[7]. Our results suggest that additional prioritization of high affinity binding and at least a moderate degree of sarbecovirus breadth will yield antibodies with improved resistance to viral escape[4,5].

A long-term goal is to develop antibodies and vaccines that cross-react with distant sarbecovirus lineages capable of zoonotic spillover. We have identified a cryptic epitope capable of eliciting pan-sarbecovirus immunity, represented by S2H97. Though S2H97-like antibodies are rare in polyclonal sera, the protective capacity and exceptional breadth of S2H97 indicates that pan-sarbecovirus vaccines could seek to improve responses to this epitope by unmasking this and other cryptic broadly neutralizing epitopes[5,37,41]. Broader cross-reactivity among betacoronavirus lineages including MERS and OC43 has been reported for antibodies that bind the spike S2 domain[32,38,42]. Though S2H97 breadth does not extend beyond sarbecoviruses, its discovery expands our view of what can be achieved via a potent RBD-directed antibody response.

The global emergence of variants of concern (VOCs) has been an important feature of the pandemic[27–29]. Mutations in VOCs occur in immunodominant RBM epitopes (e.g., residues E484, K417 and L452) and impact binding by polyclonal serum and some therapeutic antibodies[17–21]. We cannot predict exactly which mutations will next rise to prominence as SARS-CoV-2 continues to evolve, but it seems likely that they will include additional RBM mutations that impact recognition by infection- and vaccine-elicited antibodies[1,2,15,16,19]. Therefore, antibody discovery efforts focused on breadth[4,5], aided by high-resolution differentiation among antibody epitopes as generated herein, can inform the development of antibody and vaccine countermeasures with greater robustness to immune escape in the current SARS-CoV-2 pandemic and utility for potential future sarbecovirus spillovers.

MATERIALS AND METHODS

Mammalian cell lines

Cell lines were received from ATCC (Vero E6, Vero, BHK-21, CHO-K1, HEK293T/17), Takara (Lenti-X 293T) and Thermo Fisher Scientific (ExpiCHO-S, Expi293F and Freestyle 293-F). MA104 cells were a gift from Harry Greenberg. 293T-ACE2 cells are described in references [31] and [43]. Vero and MA104 cell lines tested negative for mycoplasma contamination. Other cell lines were not tested. No authentication was performed beyond manufacturer standards.

Isolation of peripheral blood mononuclear cells (PBMCs), plasma and sera

Samples from three SARS-CoV-2 recovered individuals, designated as donors S2H (age 36, male), S2D (age 70, male) and S2X (age 52, male) were obtained under study protocols approved by the local Institutional Review Board (Canton Ticino Ethics Committee, Switzerland). All donors provided written informed consent for the use of blood and blood components (such as PBMCs, sera or plasma). Blood drawn from donor S2X was obtained at day 48 (S2X16, S2X35 and S2X58 antibodies) and 75 (S2X227) after symptoms onset. Blood from donor S2H was obtained at day 17 (S2H13 and S2H14), day 45 (S2H58) and day 81 (S2H97) after symptoms onset. Blood from donor S2D was obtained at day 98 (S2D106) after symptoms onset.

PBMCs were isolated from blood draw performed using tubes pre-filled with heparin, followed by Ficoll density gradient centrifugation. PBMCs were either used fresh for SARS-CoV-2 Spike protein-specific memory B cell sorting or stored in liquid nitrogen for later use. Sera were obtained from blood collected using tubes containing clot activator, followed by centrifugation and storage at −80°C.

Sera for blockade of binding serological assays were obtained from 3 cohorts of SARS-CoV-2 convalescent (average age 52, range 25–78, 55% male) or vaccinated (average age 49, range 28–69, 65% male) individuals under study protocols approved by the local Institutional Review Boards (Canton Ticino Ethics Committee, Switzerland, the Ethical Committee of Luigi Sacco Hospital, Milan, Italy, and WCG North America, Princeton, NJ, USA). All donors provided written informed consent for the use of blood and blood components (such as PBMCs, sera or plasma) and were recruited at hospitals or as outpatients.

B-cell isolation and recombinant mAb production

Discovery and initial characterization of six antibodies in our panel was previously reported (S309 and S304[4,15], S2X35, S2H13 and S2H14[15], and S2E12[8]), and six new antibodies are first described here (S2H97, S2X16, S2H58, S2D106, S2X58, S2X227). Starting from freshly isolated PBMCs or upon cells thawing, B cells were enriched by staining with CD19 PE-Cy7 (BD Bioscience 557835, 1:50) and incubation with anti-PE MicroBeads (Miltenyi Biotec 130-048-801, 1:100), followed by positive selection using LS columns. Enriched B cells were stained with anti-IgM (BioLegend 314508, 1:20), anti-IgD (BD Bioscience 555779, 1:40), anti-CD14 (BD Bioscience 562691, 1:50) and anti-IgA (Southern Biotech 2050-09, 1:400), all PE labeled, and prefusion SARS-CoV-2 S with a biotinylated Avi-tag (in house produced) conjugated to Streptavidin Alexa-Fluor 647 (Life Technologies S21374, 1:40). SARS-CoV-2 S-specific IgG+ memory B cells were sorted by flow cytometry via gating for PE negative and Alexa-Fluor 647 positive cells. Cells were cultured for the screening of positive supernatants. Antibody VH and VL sequences were obtained by RT-PCR and mAbs were expressed as recombinant human Fab fragment or as IgG1 (G1m3 allotype) carrying the half-life extending M428L/N434S (LS) mutation in the Fc region. ExpiCHO-S cells (Thermo Fisher Scientific) were transiently transfected with heavy and light chain expression vectors as previously described[4]. Affinity purification was performed on ÄKTA Xpress FPLC (Cytiva) operated by UNICORN software version 5.11 (Build 407) using HiTrap Protein A columns (Cytiva) for full length human mAbs and CaptureSelect CH1-XL MiniChrom columns (Thermo Fisher Scientific) for Fab fragments, using PBS as mobile phase. Buffer exchange to the appropriate formulation buffer was performed with a HiTrap Fast desalting column (Cytiva). The final products were sterilized by filtration through 0.22 μm filters and stored at 4°C.

Using the Database IMGT (http://www.imgt.org), the VH and VL germline gene family and the number of somatic mutations were determined by analyzing the homology of the VH and VL sequences to known human V, D and J genes. Germline-reverted sequences of the VH and VL were constructed using IMGT/V-QUEST. The S2E12 and S2H97 germline-reverted antibodies (G1m17 allotype) were produced by ATUM. S2E12 and S2H97 germline-reverted Fabs were generated by digestion of the corresponding IgGs.

Epitope classes shown in Figs. 1a and 2g are defined as in Piccoli et al.[15] Briefly, the classification of these epitope classes results from Octet binning experiments using structurally characterized antibodies, structural insights to define the recognition of open-only RBD and ability of antibodies to interfere with RBD binding to ACE2. In particular, site Ia is accessible only in the open state of RBD and largely overlaps with ACE2 footprint; site Ib is accessible in both open and closed RBD states and overlaps in part with ACE2 footprint; site IIa is in the core RBD (accessible only in the open RBD state) and antibodies binding to this site interfere with binding to ACE2, site IIc is also in the core RBD but targeted by antibodies that do not interfere with binding to ACE2; site IV is fully accessible on both open and closed RBDs and is defined by the footprint of S309 antibody.

Neutralization of authentic SARS-CoV-2 by entry-inhibition assay

Neutralization was determined using SARS-CoV-2-Nluc, an infectious clone of SARS-CoV-2 (based on strain 2019-nCoV/USA_WA1/2020) which encodes nanoluciferase in place of the viral ORF7 and demonstrated comparable growth kinetics to wildtype virus[44]. Vero E6 cells (ATCC, CRL-1586) were seeded into black-walled, clear-bottom 96-well plates at 2×10^4 cells/well and cultured overnight at 37°C. The next day, 9-point 4-fold serial dilutions of mAbs were prepared in infection media (DMEM + 10% FBS). SARS-CoV-2-Nluc was diluted in infection media at a final MOI of 0.01 PFU/cell, added to the mAb dilutions and incubated for 30 minutes at 37°C. Media was removed from the Vero E6 cells, mAb-virus complexes were added and incubated at 37°C for 24 hours. Media was removed from the cells, Nano-Glo luciferase substrate (Promega) was added according to the manufacturer's recommendations, incubated for 10 minutes at room temperature and the luciferase signal was quantified on a VICTOR Nivo plate reader (Perkin Elmer).

SARS-CoV-2 spike pseudotyped VSV generation and neutralization assay

Replication defective VSV pseudoviruses[45] expressing SARS-CoV-2 spike protein were generated as previously described[46] with some modifications. Plasmids encoding SARS-CoV-2 spike single-mutant variants were generated by site-directed mutagenesis of the wild-type plasmid, pcDNA3.1(+)-spike-D19[47], and plasmids encoding multiply mutated SARS-CoV-2 variants of concern were generated using a multistep overlap extension PCR protocol[23,48], in which sequential, overlapping fragments were designed to introduce all mutations, which were PCR assembled and cloned into the pcDNA3.1 vector using the Takara In-fusion HD cloning kit following manufacturer's instructions.

Lenti-X 293T (Takara, 632180) cells were seeded in 10-cm dishes at a density of 1×10^5 cells/cm^2 and the following day transfected with 5 μg of spike expression plasmid with TransIT-Lenti (Mirus, 6600) according to the manufacturer's instructions. For the neutralization assays with variants of concern (Figs. 2d, 3b), Lenti-X 293T cells were seeded in 10-cm dishes at a density of 5×10^6 cells/cm^2, and transfected the following day with 10 μg of spike expression plasmid. One day post-transfection, cells were infected with VSV (G*ΔG-luciferase) (Kerafast, EH1020-PM) for 1 h, rinsed three times with PBS, then incubated for an additional 24 h in complete media at 37°C. The cell supernatant was clarified by centrifugation, filtered (0.45 μm), aliquoted, and frozen at −80°C.

For VSV pseudovirus neutralization assays, Vero E6 cells (ATCC, CRL-1586) were grown in DMEM supplemented with 10% FBS and seeded into clear bottom white 96 well plates (Costar, 3903) at a density of 2×10^4 cells per well. The next day, mAbs were serially diluted in pre-warmed complete media, mixed at a 1:1 ratio with pseudovirus and incubated for 1 h at 37°C in round bottom polypropylene plates. Media from cells was aspirated and 50 μL of virus-mAb complexes were added to cells and then incubated for 1 h at 37°C. An additional 100 μL of prewarmed complete media was then added on top of complexes and cells incubated for an additional 16–24 h. Conditions were tested in duplicate wells on each plate and at least six wells per plate contained uninfected, untreated cells (mock) and infected, untreated cells ('no mAb control').

Virus-mAb-containing media was then aspirated from cells and 100 μL of a 1:4 dilution of Bio-glo (Promega, G7940) in PBS was added to cells. For neutralization assays with variants of concern, 50 μL of a 1:2 dilution of SteadyLite Plus (Perkin Elmer) in PBS with $Ca^{2+}Mg^{2+}$ was added to cells in place of Bio-glo. Plates were incubated for 10 min at room temperature and then were analyzed on the Envision plate reader (PerkinElmer), or for variants of concern assays, a Synergy H1 Hybrid Multi-Mode reader (Biotek).

Relative light units (RLUs) for infected wells were subtracted by the average of RLU values for the mock wells (background subtraction) and then normalized to the average of background subtracted "no mAb control" RLU values within each plate. Percent neutralization was calculated by subtracting from 1 the normalized mAb infection condition. Data were analyzed and visualized with Prism (Version 8.4.3). IC_{50} values were calculated from the interpolated value from the log(inhibitor) versus response – variable slope (four parameters) nonlinear regression with an upper constraint of < 100. Neutralization experiments with wildtype SARS-CoV-2 S and single-mutant variants were conducted on three independent days, i.e., biological replicates, where each biological replicate contains a technical duplicate. IC_{50} values across biological replicates are presented as geometric mean. The loss or gain of neutralization potency across spike variants was calculated by dividing the variant IC_{50} by the parental IC_{50} within each biological replicate. Neutralization experiments with SARS-CoV-2 S variants of concern were conducted in biological duplicates, with IC50 values normalized by the corresponding wildtype measurement, and presented as arithmetic mean of the duplicate experiments.

SARS-CoV-2 spike pseudotyped VSV neutralization on 293T-ACE2 cells

To investigate the effect of ACE2 expression on S2H97 neutralization, Vero E6 cells were seeded at 20,000 cells per well in black clear-bottom 96-well plates. 293T-ACE2 cells[31] were seeded at 35,000 cells per well in black clear-bottom 96-well plates that had been pre-coated with poly-D-Lysine (Gibco). The next day, SARS-CoV-2 spike-pseudotyped VSV neutralizations with S2E12, S309 and S2H97 were performed as described above. Neutralizations were performed in triplicate wells.

Sarbecovirus spike pseudotyped VSV neutralization by S2H97

Mammalian expression constructs (pcDNA3.1(+) or pTwist-CMV) encoding the spike proteins from various sarbecoviruses with a C-terminal deletion of 19 amino acids (D19) were synthesized for SARS-CoV-2 (Genbank: QOU99296.1), SARS-CoV-1 Urbani (Genbank: AAP13441.1), hCoV-19/pangolin/Guangdong/1/2019 (GD-Pangolin-CoV, Genbank: QLR06867.1), Pangolin coronavirus Guanxi-2017 (GX-Pangolin-CoV, Genbank: QIA48623.1), and bat sarbecovirus WIV1 (WIV1, Genbank: AGZ48828.1). Lenti-X 293T cells (Takara, 632180) were seeded in 15 cm dishes such that the cells would reach 80% confluency after culturing overnight. The following day, cells were transfected using TransIT-Lenti (Mirus, 6600) according to the manufacturer's instructions. One day post-transfection, cells were infected with VSV (G*ΔG-luciferase) (Kerafast, EH1020-PM). The supernatant containing sarbecovirus pseudotyped VSV was collected 2 days post-transfection, centrifuged at 1000 × g for 5 minutes, aliquoted and frozen at −80°C.

For neutralization assays, cells supporting robust pseudovirus infection were seeded into clear bottom white-walled 96-well plates at 20,000 cells/well in 100 μL culture media. Vero E6 cells were used for VSV-SARS-CoV-2, VSV-SARS-CoV-1, and VSV-GD-Pangolin-CoV. BHK-21 cells (ATCC, CCL-10) stably expressing ACE2 were used for VSV-GX-Pangolin-CoV and VSV-WIV1. After culturing cells overnight, 1:3 serial dilutions of antibody were prepared in DMEM in triplicate. Pseudovirus was diluted in DMEM and added to each antibody dilution such that the final dilution of pseudovirus was 1:20. Pseudovirus:antibody mixtures were incubated for 1 hour at 37°C. Media was removed from the cells and 50 μL of pseudovirus:antibody mixtures were added. One hour post-infection, 50 μL of culture media was added to wells containing pseudovirus:antibody mixtures and incubated overnight at 37°C. Media was then removed and 100 μL of 1:1 diluted DPBS:Bio-Glo (Promega, G7940) luciferase substrate was added to each well. The plate was shaken at 300 RPM at room temperature for 10 minutes after which RLUs were read on an EnSight (Perkin Elmer) microplate reader. Percent neutralization was determined by first subtracting the mean background (cells with luciferase substrate alone) RLU values of 6 wells per plate for all data points. Percent neutralization for each antibody concentration was calculated relative to no antibody control wells for each plate. Percent neutralization data were analyzed and graphed using Prism (GraphPad, v9.0.1). Absolute IC_{50} values were calculated by fitting a curve using a non-linear regression model (variable slope, 4 parameters) and values were interpolated from the curve at y=50. The geometric mean from at least two independent experiments was calculated using Excel (Microsoft, Version 16.45).

Sarbecovirus spike pseudotyped VSV neutralization by S2E12

Spikes from SARS-CoV-2 (CAD0240757.1), RaTG13 (QHR63300.2), GD-Pangolin (QLR06867.1), GX-Pangolin (QIA48623.1), SARS-CoV-1 Tor2 (YP009825051), WIV1 (AGZ48831.1) and WIV16 (ALK02457.1) were used to pseudotype VSV. To produce pseudotyped viruses, HEK293T/17 (ATCC, CRL-11268) seeded in 10 cm dishes in DMEM supplemented with 10% FBS, 1% PenStrep were transfected with plasmids using lipofectamine 2000 (Life Technologies) following manufacturer’s instructions. One day post-transfection, cells were infected with VSV (G*ΔG-luciferase) for 2 h and washed four times with DMEM, before adding medium supplemented with anti-VSV-G antibody (I1-mouse hybridoma supernatant at 1:50 dilution, from CRL-2700, ATCC). Pseudotyped particles were harvested 18 h post-inoculation, clarified by centrifugation at 2000×g for 5 min, concentrated 10× with a 30 kDa cutoff membrane filter, and stored at −80°C. For S2E12 neutralization experiments, 293T cells stably expressing ACE2 (BEI #NR-52511)[43] in DMEM supplemented with 10% FBS and 1% PenStrep were seeded at 40,000 cells/well in clear-bottom white-walled 96-well plates and cultured overnight at 37°C. Twelve 3-fold serial dilutions of S2E12 antibody were prepared in DMEM, and antibody dilutions were mixed 1:1 with pseudotyped VSV in the presence of 1:50 diluted anti-VSV-G antibody. After 45 min incubation at 37°C, 40 μL of antibody-virus mixture was added to cells, and 40 μL DMEM was added 2 h post-infection. After 17–20 h, 50 μL One-Glo-EX substrate (Promega) was added to the cells. Cells were incubated in the dark for 5–10 min prior to luminescence reading on a Varioskan LUX plate reader (Thermo Fisher Scientific). Relative luciferase unit values were converted to percentage of neutralization and plotted with a nonlinear regression curve fit in GraphPad Prism. Measurements were performed in duplicate with two independent productions of pseudotyped virus.

Recombinant protein production

SARS-CoV-2 RBD WT proteins for SPR binding assays (with N-terminal signal peptide and C-terminal thrombin cleavage site-TwinStrep-8xHis-tag) were expressed in Expi293F (Thermo Fisher Scientific) cells at 37°C and 8% CO_2. Transfections were performed using the ExpiFectamine 293 Transfection Kit (Thermo Fisher Scientific). Cell culture supernatants were collected three days after transfection and supplemented with 10x PBS to a final concentration of 2.5x PBS (342.5 mM NaCl, 6.75 mM KCl and 29.75 mM phosphates). SARS-CoV-2 RBDs were purified using 1 or 5 mL HisTALON Superflow cartridges (Takara Bio) and subsequently buffer exchanged into 1x HBS-N buffer (Cytiva) or PBS using a Zeba Spin Desalting (Thermo Fisher Scientific) or HiPrep 26/10 (Cytiva) desalting column.

SARS-CoV-2 RBD WT for crystallization (with N-terminal signal peptide and ‘ETGT’, and C-terminal 8xHis-tag) was expressed similarly as described above in the presence of 10 μM kifunensine. Cell culture supernatant was collected four days after transfection and supplemented with 10x PBS to a final concentration of 2.5x PBS. Protein was purified using a 5 ml HisTALON Superflow cartridge followed by size exclusion chromatography on a Superdex 200 Increase 10/300 GL column (Cytiva) equilibrated in 20 mM Tris-HCl pH 7.5, 150 mM NaCl. For crystallization of the RBD-S2X259-S2H97 and RBD-S2E12-S304-S309 Fab complexes, RBD was deglycosylated by overnight incubation with EndoH glycosidase at 4°C.

RBDs from other sarbecoviruses for SPR (with N-terminal signal peptide and C-terminal thrombin cleavage site-TwinStrep-8xHis-tag) were expressed in Expi293F cells at 37°C and 8% CO_2. Cells were transfected using PEI MAX (Polysciences) at a DNA:PEI ratio of 1:3.75. Transfected cells were supplemented three days after transfection with 3 g/L glucose (Bioconcept) and 5 g/L soy hydrolysate (Sigma-Aldrich Chemie GmbH). Cell culture supernatant (423 mL) was collected seven days after transfection and supplemented with 47 mL 10x binding buffer (1 M Tris-HCl, 1.5 M NaCl, 20 mM EDTA, pH 8.0) and 25 mL BioLock (IBA GmbH) and incubated on ice for 30 min. Proteins were purified using a 5 mL Strep-Tactin XT Superflow high capacity cartridge (IBA GmbH) followed by buffer exchange to PBS using HiPrep 26/10 desalting columns (Cytiva).

Prefusion-stabilized SARS-CoV-2 spike proteins for SPR (residues 14–1211, either D614 or D614G), containing the 2P and Furin cleavage site mutations[49] with a mu-phosphatase signal peptide and a C-terminal Avi-8xHis-C-tag or C-terminal 8xHis-Avi-C-tag were expressed in Freestyle 293-F cells (Thermo Fisher Scientific, R79007) at 37°C and 8% CO_2. Transfections were performed using 293fectin as a transfection reagent. Cell culture supernatant was collected after three days and purified over a 5 mL C-tag affinity matrix. Elution fractions were concentrated and injected on a Superose 6 Increase 10/300 GL column (Cytiva) with 50 mM Tris-HCl pH 8.0 and 200 mM NaCl as running buffer.

SARS-CoV-2 HexaPro spike protein for cryoEM analysis was produced in Freestyle 293-F cells grown in suspension using FreeStyle 293 expression medium (Life Technologies) at 37°C in a humidified 8% CO_2 incubator rotating at 130 RPM. The cultures were transfected using PEI (9 µg/mL) with cells grown to a density of 2.5 million cells per mL and cultivated for three days. The supernatants were harvested and cells resuspended for another three days, yielding two harvests. Spike proteins were purified from clarified supernatants using a 5 mL Cobalt affinity column (Cytiva, HiTrap TALON crude), concentrated and flash frozen in a buffer containing 20 mM Tris pH 8.0 and 150 mM NaCl prior to analysis.

SARS-CoV-2 S native-like ectodomain trimer for refolding assays was engineered with a mu-phosphatase signal peptide beginning at 14Q, a mutated S1/S2 cleavage site (SGAR), and a TEV cleavage, fold-on trimerization motif, and 8x His tag appended to the C-terminus (K1211). Native-like spike was expressed and purified as described for SARS-CoV-2 HexaPro spike above.

Recombinant hACE2 for SPR (residues 19–615 from Uniprot Q9BYF1 with a C-terminal AviTag-10xHis-GGG-tag, and N-terminal signal peptide) was produced by ATUM. Protein was purified via Ni Sepharose resin followed by isolation of the monomeric hACE2 by size exclusion chromatography using a Superdex 200 Increase 10/300 GL column (Cytiva) pre-equilibrated with PBS.

SPR binding assays

SPR binding measurements were performed using a Biacore T200 instrument with CM5 sensor chip covalently immobilized with StrepTactin XT to capture recombinant RBD proteins (data in Fig. 1a and Extended Data Fig. 4f,i,l). Running buffer was Cytiva HBS-EP+ (pH 7.4). All measurements were performed at 25°C. Fab (or hACE2) analyte concentrations were 11, 33, 100, and 300 nM, run as single-cycle kinetics. Double reference-subtracted data were fit to a 1:1 binding model using Biacore T200 Evaluation (version 3.1) or Biacore Insight Evaluation (version 2.0.15) software. K_D above 1 µM were determined from fits where Rmax was set as a constant based on results for higher affinity analytes binding to the same RBD at the same surface density. Data are representative of duplicate or triplicate measurements (except measurements with germline Fabs were singleton measurements).

To corroborate the SARS-CoV-2 RBD binding measurements, experiments were also performed in two additional formats, both with monovalent analytes (data in Extended Data Table 1): (1) Fab binding to SARS-CoV-2 spike ectodomain was measured using CM5 sensor chips immobilized with anti-AviTag pAb (Genscript, A00674-40) for capturing S, other experiment parameters same as above, and (2) RBD binding to IgG was measured using CM5 sensor chips immobilized with anti-human Fc pAb (Southern Biotech, 2014–01) for capturing IgG, with RBD analyte concentrations of 3.1, 12.5, and 50 nM, other experiment parameters same as above. Fit results yield an “apparent K_D” for the spike-binding experiments because the kinetics also reflect spike conformational dynamics. Spike ectodomain was D614G with C-terminal 8xHis-Avi-C-tag for all measurements except S2X58 binding was performed with D614 spike with C-terminal Avi-8xHis-C-tag. For the comparison of mature and germline-reverted antibody binding to RaTG13, the data reported are from experiment format (2) with IgG as ligand. These data were fit to a Heterogeneous Ligand model, due to an artifactual kinetic phase with very slow dissociation that often arises when RBD is an analyte; the lower affinity of the two K_Ds reported by the fit is given as the K_D (the two K_Ds are separated by at least one order of magnitude).

Deep mutational scanning mutant escape profiling

We used a previously described deep mutational scanning approach[3] to comprehensively identify RBD mutations that escape binding by each antibody. This approach leverages duplicate RBD mutant libraries[26], which contain virtually all of the 3,819 possible amino acid mutations in the background of the Wuhan-Hu-1 RBD sequence. Library variants were previously linked to short identifier barcode sequences and sorted to purge the library of variants that strongly decrease ACE2 binding affinity or expression of folded RBD[3].

We first used an isogenic yeast strain expressing the unmutated SARS-CoV-2 RBD and flow cytometry to identify the EC90 of each antibody's binding to yeast-displayed SARS-CoV-2 RBD. We then performed library selections as previously described[3,20], labeling libraries with the EC90 concentration of antibody to standardize escape mutation sensitivity across selections. Briefly, libraries of yeast were induced for surface expression, washed, and labeled with the primary antibody for one hour at room temperature. Cells were washed, and secondarily labeled with 1:200 PE-conjugated goat anti-human-IgG antibody (Jackson ImmunoResearch 109-115-098) to label for bound antibody, and 1:100 FITC-conjugated chicken anti-Myc-tag (Immunology Consultants Lab, CYMC-45F) to label for RBD surface expression. We prepared controls for setting FACS selection gates by labeling yeast expressing the unmutated SARS-CoV-2 RBD with the same antibody concentration as library selections (1x), 100x reduced antibody concentration to illustrate the effect of mutations with 100x-reduced affinity, and 0 ng/mL antibody to illustrate complete loss of antibody binding. Representative selection gates are shown in Extended Data Fig. 2b. Gates were set and sorting performed with FACSDiva software (version 6.1.3). We sorted approximately 7.5×10^6 RBD+ cells per library on a BD FACSAria II, collecting yeast cells from the antibody-escape sort bin (fractions of library falling into antibody escape bin given in Extended Data Fig. 2c). Sorted cells were recovered overnight, plasmids were extracted from the pre-sort and antibody-escape populations, and variant-identifier barcode sequences were PCR amplified and sequenced on an Illumina HiSeq 2500[3,26].

As previously described[3,20], sequencing counts pre- and post-selection were used to estimate the "escape fraction" for each library variant, which reflects the fraction of yeast expressing a variant that fall into the antibody-escape FACS bin. Briefly, we used the dms_variants package (https://jbloomlab.github.io/dms_variants/, version 0.8.2) to process Illumina sequences into variant counts pre- and post-selection using the barcode/RBD variant lookup table from Starr et al.[26]. We then computed per-variant escape fractions as: $E_v = F \times (n_v^{post} / N_{post}) / (n_v^{pre} / N_{pre})$, where F is the total fraction of the library that escapes antibody binding (Extended Data Fig. 2c), n_v^{post} and n_v^{pre} are the sequencing counts of variant v in the RBD library after and before FACS selection (with a pseudocount of 0.5 added to all counts), and N_{post} and N_{pre} are the total counts of all variants after and before FACS selection. We then applied computational filters to remove variants with low pre-sort sequencing counts or highly deleterious mutations that might cause artefactual antibody escape due to global unfolding or loss of expression of RBD on the cell surface. Specifically, we filtered out variants whose pre-selection sequencing counts were lower than the 99th percentile counts of variants containing premature stop codons, which were largely purged by the prior sorts for RBD expressing and ACE2-binding RBD variants. We also removed variants with ACE2 binding scores < -2.35 or RBD expression scores < -1, and variants containing individual mutations with effects below these thresholds, using the variant- and mutation-level deep mutational scanning measurements of Starr et al.[26]. We also filtered out rare mutations with low coverage in the libraries, retaining mutations that were sampled on at least one single-mutant barcoded variant or at least two multiply-mutated variants in each replicate. Last, to decompose single-mutation escape fractions for each antibody, we implemented global epistasis models[50] using the dms_variants package to estimate the effect of each individual amino acid mutation, exactly as described in ref. [20].

Antibody escape selections were conducted in full duplicate using independently generated and assayed SARS-CoV-2 mutant libraries (see correlations in Extended Data Fig. 2e,f). The reported escape fractions throughout the paper are the average across the two replicates, and these final per-mutation escape fractions are provided on GitHub: https://github.com/jbloomlab/SARS-CoV-2-RBD_MAP_Vir_mAbs/blob/main/results/supp_data/vir_antibodies_raw_data.csv. Interactive visualizations of antibody escape maps (https://jbloomlab.github.io/SARS-CoV-2-RBD_MAP_Vir_mAbs) were created using dms-view[51].

Sarbecovirus library binding assays

A curated set of all unique sarbecovirus RBD amino acid sequences was gathered, including the sarbecovirus RBD sequence set reported by Letko et al.[7], along with additional unique RBD sequences among SARS-CoV-1 epidemic strains reported by Song et al.[52], BtKY72[53] and new sarbecovirus sequences RmYN02[54], GD-Pangolin-CoV (consensus RBD reported in Fig. 3a of Lam et al.[55]), and GX-Pangolin-CoV[55] (P2V, ambiguous nucleotide within codon 515 (SARS-CoV-2 spike numbering) resolved to retain F515, which is conserved in all other sarbecoviruses). A list of all RBDs and sequence accession numbers is available on GitHub: https://github.com/jbloomlab/SARSr-CoV_RBD_MAP/blob/main/data/RBD_accessions.csv

To define clades of sarbecovirus RBDs, an alignment of amino acid RBD sequences was generated using mafft[56] with gap opening penalty 4.5 (alignment available on GitHub: https://github.com/jbloomlab/SARSr-CoV_RBD_MAP/blob/main/data/RBD_aa_aligned.fasta). The corresponding nucleotide sequence alignment was generated from the amino acid alignment using PAL2NAL[57]. The gene sequence phylogeny was inferred using RAxML version 8.2.12[58], with the GTRGAMMA substitution model and a partition model with separate parameters for first, second, and third codon positions. The Hibecovirus RBD sequence Hp-Zhejiang2013 (Genbank: KF636752) was used as an outgroup for rooting of the sarbecovirus phylogeny.

All unique sarbecovirus RBD protein-coding sequences were ordered from IDT, Twist, and Genscript, and cloned into our yeast display vector[26]. Sequences were pooled and appended with downstream 16-nt barcode sequences according to the protocol described in Starr et al.[26]. Long read circular consensus sequences spanning the 16-nt barcode and RBD genotype were gathered on a PacBio Sequel v2.0 and processed exactly as described in Starr et al.[26]. This yielded a barcode:variant lookup table for the sarbecovirus RBD library analogous to that used for SARS-CoV-2 mutant libraries. This table is available on GitHub: https://github.com/jbloomlab/SARSr-CoV_RBD_MAP/blob/main/data/barcode_variant_table.csv.

The pooled sarbecovirus RBD library was labeled, sorted, and quantified as described for the SARS-CoV-2 mutant libraries above, except we only sorted ~1 million RBD+ cells due to the reduced library size. Sequencing and quantification of per-variant antibody escape was conducted as described above. Data for the HKU3-8 RBD is not shown, as this RBD did not express in our yeast-display platform. For several antibodies, we performed a secondary experiment, selecting the sarbecovirus RBD library with a more stringent “full escape” gate to select out only variants exhibiting complete loss of binding (Extended Data Fig. 2b,c).

For follow-up quantitative binding assays, select sarbecovirus RBDs were cloned into the yeast-display platform as isogenic stocks. Binding assays were conducted across a titration series of antibody in 96-well plates, and binding at each antibody concentration (geometric mean fluorescence intensity in the PE channel among RBD+ (FITC+) cells) was determined via flow cytometry and fit to a four-parameter Hill curve to identify the EC50 (midpoint).

Analysis of mutations in natural SARS-CoV-2 sequences

All spike sequences on GISAID[59] as of May 2, 2021, were downloaded and aligned via mafft[56]. Sequences from non-human origins, sequences with gaps or ambiguous characters in the RBD, and sequences with more than 8 amino acid differences from the Wuhan-Hu-1 reference sequence (Genbank MN908947, residues N331-T531) were removed. We determined mutation frequencies compared to Wuhan-Hu-1 reference from this final alignment of 1,190,241 sequences. We acknowledge all contributors to the GISAID EpiCoV database for their sharing of sequence data. All contributors to GISAID EpiCoV listed at: https://github.com/jbloomlab/SARS-CoV-2-RBD_MAP_Vir_mAbs/blob/main/data/gisaid_hcov-19_acknowledgement_table_2021_03_04.pdf.

Quantitative summary metrics of antibody properties

The relative epitope size of an antibody was calculated as the sum of per-mutant escape fractions that are at least five times the global median escape fraction (to minimize the impact of variation in background noise on the summation). For this summation, escape fractions were normalized to the maximum per-mutation escape fraction, to account for slight variation in the largest per-mutation escape fraction measured between selections.

The relative escapability of an antibody was calculated the same as relative epitope size, but each mutation was multiplied by two weighting factors scaled from 0 to 1 that reflect the impact of that mutation on ACE2-binding affinity and RBD expression as measured in our prior deep mutational scan[26]. The relationship between weighting factors and mutation effect on each property is shown in Extended Data Fig. 3a. Mutations with < -1 effect on either property are effectively zeroed out in the escapability summation. Mutations with effects between −1 and 0 have intermediate weights, and mutations with 0 or positive effects are assigned weight factors of 1.

Antibody susceptibility to escape by natural SARS-CoV-2 mutations was calculated as the summed GISAID frequencies of all escape mutations, where escape mutations (all labels in Extended Data Fig. 3c) are defined as those with escape fraction greater than five times the median escape fraction as above. These summed natural escape frequencies are tabulated in the plot headers in Extended Data Fig. 3c.

The summary breadth of an antibody was calculated from the sarbecovirus RBD library escape selection using the standard gating (Extended Data Fig. 4b), only. Although we have various follow-up binding data illustrating reduced affinity binding for some “escaped” sarbecovirus RBDs, these follow-up experiments were not conducted systematically for all antibody/RBD combinations, and therefore would bias breadth estimates. Breadth of binding was calculated as the frequency of all sarbecovirus RBDs that are bound with affinity within the FACS selection gating threshold, weighted by clade representation. Breadth was normalized to give equal representation to each of the four sarbecovirus clades to account for different depth of sampling. Within the SARS-CoV-1 clade, all human 02/03 strains and civet + human 03/04 strains were similarly down-weighted to each represent 1/8 of the possible breadth within the SARS-CoV-1 clade (together with the six bat sarbecoviruses in this clade). As an example, breadth for S304 is calculated as [4/4 +([6/6]+[6/6]+5)/8 + 2/2 + 0/21]/4 = 0.72, based on the data shown in Extended Data Fig. 4b.

Multidimensional scaling projection of antibody epitopes

Multidimensional scaling projection in Fig. 4 was performed using the Python scikit-learn package. We first computed the similarity and dissimilarity in the sites of escape between each pair of antibodies, exactly as described in Greaney et al.[3], and performed metric multidimensional scaling with two components on the matrix of dissimilarities between all antibody pairs. Antibodies in this layout were colored with pie charts proportional to the total squared site-wise escape that falls into the labeled structural regions (RBM = residues 437 to 508, ACE2 contact defined as 4Å cutoff based on 6M0J crystal structure[60], and core RBD otherwise). In this layout, we included all of our previously published antibodies for which we have performed escape mapping via this same approach. These antibodies and their citations include: S2X259[37]; LY-CoV555[21]; COV2-2196 and COV2-2130[36]; REGN10933, REGN10987, and LY-CoV016[20]; and all other COV2 antibodies and CR3022[3].

For Fig. 4b–d and Extended Data Fig. 7c, we colored the antibodies within this layout according to various antibody properties. When appropriate, we also colored these previously assayed antibodies, as described below. Extended Data Fig. 7d and the scatterplots in Fig. 4e–g show the relationships between properties for antibodies specifically in this study (and S2X259) for the most direct comparability.

Antibody neutralization potencies illustrated in Fig. 4b incorporate the authentic SARS-CoV-2 neutralization IC50s as reported in this study (Fig. 1a), together with the live SARS-CoV-2 neutralization IC50s for the COV2 antibodies reported by Zost et al.[10]. We acknowledge that it is imperfect to compare neutralization potencies reported from different labs on different antibody batches, though in this case, both sets are indeed neutralization potencies with authentic virus. We therefore do not directly compare these two sets of measurements in a quantitative manner, but we do note that their joint inclusion in Fig. 4b supports the dichotomy between neutralization potency of core RBD versus RBM antibodies which is supported by either neutralization panel alone.

Sarbecovirus breadth illustrated in Fig. 4c incorporates the pan-sarbecovirus breadth measurements reported in the current study together with more limited breadth measurements for antibodies reported in our prior publications. These previously published experiments determined binding within a more restricted sarbecovirus RBD set present in our libraries (SARS-CoV-2, RaTG13, GD-Pangolin, SARS-CoV-1 [Urbani], LYRa11, and WIV1). We calculated breadth from this incomplete sarbecovirus sequence set for comparison, but note that these antibodies are limited to a relative breadth of 0.5 because no RBDs from the Africa/Europe or non-ACE2-utilizing Asia clades were included. However, as with neutralization, inclusion of these antibodies nonetheless emphasizes the core RBD/RBM dichotomy in sarbecovirus breadth established by our primary panel.

For illustrations of epitope size and escapability in Fig. 4d and Extended Data Fig. 7c, we calculated these quantities for our previously profiled antibodies as described above. We excluded the antibodies profiled in Greaney et al.[3], as these assays were performed on a prior version of our SARS-CoV-2 mutant library that exhibited different quantitative features of absolute escape, complicating its quantitative comparison to extent of escape for antibodies profiled in this and our other studies, which all use the same library.

Structural mappings around the perimeter of Fig. 4a were created by mapping total site-wise escape to the b-factor column of PDB structures. Footprints were defined as residues within a 5Å cutoff of antibody heavy atoms. Structures used were those described in this paper, or previously published structures: ACE2-bound RBD (6M0J)[60], CR3022-bound RBD (6W41)[61], REGN10987- and REGN10933-bound RBD (6XDG)[62], CB6- (LY-CoV016) bound RBD (7C01)[63], and S304, S309, and S2H14-bound RBD (7JX3)[15].

RBD ELISA

96 half area well-plates (Corning, 3690) were coated over-night at 4°C with 25 μL of sarbecoviruses RBD proteins at 5 μg/mL in PBS pH 7.2. Plates were blocked with PBS 1% BSA (Sigma-Aldrich, A3059) and subsequently incubated with mAb serial dilutions for 1 h at room temperature. After 4 washing steps with PBS 0.05% Tween 20 (PBS-T) (Sigma-Aldrich, 93773), goat anti-human IgG secondary antibody (Southern Biotech, 2040–04) was added and incubated for 1 h at room temperature. Plates were then washed 4 times with PBS-T and 4-NitroPhenyl phosphate (pNPP, Sigma-Aldrich, 71768) substrate added. After 30 min incubation, absorbance at 405 nm was measured by a plate reader (Biotek) and data plotted using Prism GraphPad.

Binding to cell surface expressed sarbecovirus S proteins by flow cytometry

ExpiCHO-S cells were seeded at 6 × 10^6 cells cells/mL in a volume of 5 mL in a 50 mL bioreactor. Spike coding plasmids were diluted in cold OptiPRO SFM, mixed with

ExpiFectamine CHO Reagent (Life Technologies) and added to the cells. Transfected cells were then incubated at 37°C with 8% CO_2 with an orbital shaking speed of 120 RPM (orbital diameter of 25 mm) for 42 hours. Transiently transfected ExpiCHO-S cells were harvested and washed two times in wash buffer (PBS 1% BSA, 2 mM EDTA). Cells were counted and distributed into round bottom 96-well plates (Corning) and incubated with 10 µg/mL S2H97, S2X35 or S309 mAb. Alexa Fluor647-labelled Goat Anti-Human IgG secondary Ab (Jackson ImmunoResearch 109-607-003) was prepared at 1.5 µg/mL added onto cells after two washing steps. Cells were then washed twice and resuspended in wash buffer for data acquisition on a ZE5 cytometer (Biorad).

Crystallization, data collection, structure determination, and analysis

To form RBD-Fab complexes for crystallization, SARS-CoV-2 RBD was mixed with a 1.3-fold molar excess of each Fab and incubated on ice for 20–60 min. Complexes were purified on a Superdex 200 Increase 10/300 GL column (Cytiva) preequilibrated with 20 mM Tris-HCl pH 7.5 and 150 mM NaCl. Crystals of the RBD-Fab complexes were obtained at 20°C by sitting drop vapor diffusion.

For the SARS-CoV-2 RBD-S2X35-S309 complex, a total of 200 nL complex at 5.4 mg/mL was mixed with 100 nL mother liquor solution containing 1.85 M Ammonium Sulfate, 0.1 M Tris pH 8.17, 0.8% (w/v) polyvinyl alcohol, 1% (v/v) 1-propanol, and 0.01 M HEPES pH 7. Crystals were flash frozen in liquid nitrogen using the mother liquor solution supplemented with 20% glycerol for cryoprotection. Data were collected at Beamline 9–2 of the Stanford Synchrotron Radiation Lightsource facility in Stanford, CA and processed with the XDS software package (version Jan 31, 2020)[64] to 1.83 Å in space group C222. The RBD-S2X35-S309 Fab complex structure was solved by molecular replacement using phaser[65] from a starting model consisting of RBD-S309 Fab (PDB ID: 7JX3) and a homology model for the S2X35 Fab built using the Molecular Operating Environment (MOE) software package from the Chemical Computing Group (https://www.chemcomp.com).

For the SARS-CoV-2-RBD-S2H97-S2X259 Fab complex, 200 nL complex at 5.7 mg/mL were mixed with 200 nL mother liquor solution containing 0.12 M Monosaccharides mix, 20% (v/v) Ethylene glycol, 10% (w/v) PEG 8000, 0.1 M Tris (base)/bicine pH 8.5, 0.02 M Sodium chloride, 0.01 M MES pH 6 and 3% (v/v) Jeffamine ED-2003. Crystals were flash frozen in liquid nitrogen. Data were collected at Beamline 9–2 of the Stanford Synchrotron Radiation Lightsource facility in Stanford, CA. Data were processed with the XDS software package (version Jan 31, 2020)[64] for a final dataset of 2.65 Å in space group $P2_1$. The RBD-S2H97-S2X259 Fab complex structure was solved by molecular replacement using phaser from a starting model consisting of SARS-CoV-2 RBD (PDB ID: 7JX3) and homology models for the S2H97 and S2X259 Fabs built using the MOE software package.

For the SARS-CoV-2-RBD-S2E12-S304-S309 Fab complex, 200 nL complex at 4.5 mg/mL were mixed with 100 nL of 0.09 M Phosphate/Citrate pH 5.5, 27% (v/v) PEG Smear Low, 4% (v/v) Polypropylene glycol 400 and 0.02 M Imidazole pH 7 or 100 nL of 0.09 M Phosphate/Citrate pH 5.5, 27% (v/v) PEG Smear Low, 0.01 M Potassium/sodium phosphate pH 7, 1% (v/v) PPGBA 230 and 1.5% (v/v) PPGBA 400. Crystals were flash frozen in liquid nitrogen. Data were collected at the Molecular Biology Consortium beamline 4.2.2 at the Advanced Light Source synchrotron facility in Berkeley, CA. Datasets from two crystals from the two conditions were individually processed and then merged with the XDS software package (version Jan 31, 2020)[64] for a final dataset of 2.93 Å in space group $I4_122$. The RBD-S2E12-S304-S309 Fab complex structure was solved by molecular replacement using phaser from starting models consisting of RBD-S304-S309 Fab (PDB ID: 7JX3) and S2E12 (PDB ID: 7K3Q).

For all structures, several subsequent rounds of model building and refinement were performed using Coot (version 0.9.5)[66], ISOLDE (ChimeraX version 1.1/ISOLDE version 1.1)[67], Refmac5 (version 5.8.0267)[68], and MOE (version 2019.0102) (https://www.chemcomp.com), to arrive at the final models. For all complexes, epitopes on the RBD protein were determined by identifying all RBD residues within a 5.0 Å distance from any Fab atoms. The analysis was performed using the MOE software package and the results were manually confirmed.

Cryo-electron microscopy

SARS-CoV-2 HexaPro S[69] at 1.2 mg/mL was incubated with 1.2 fold molar excess of recombinantly purified S2D106 or S2H97 at 4°C before application onto a freshly glow discharged 2.0/2.0 UltrAuFoil grid (200 mesh). Plunge freezing used a vitrobot MarkIV (Thermo Fisher Scientific) using a blot force of 0 and 6.5 second blot time at 100% humidity and 23°C.

For the S/S2D106 data set, Data were acquired using an FEI Titan Krios transmission electron microscope operated at 300 kV and equipped with a Gatan K2 Summit direct detector and Gatan Quantum GIF energy filter, operated in zero-loss mode with a slit width of 20 eV. Automated data collection was carried out using Leginon[70] at a nominal magnification of 130,000x with a pixel size of 0.525 Å. The dose rate was adjusted to 8 counts/pixel/s, and each movie was acquired in super-resolution mode fractionated in 50 frames of 200 ms. 2,166 micrographs were collected with a defocus range between −0.5 and −2.5 μm. Movie frame alignment, estimation of the microscope contrast-transfer function parameters, particle picking, and extraction were carried out using Warp[71]. Particle images were extracted with a box size of 800 binned to 400 pixelŝ2 yielding a pixel size of 1.05 Å.

For the S/S2H97 data set, data were acquired on an FEI Glacios transmission electron microscope operated at 200 kV equipped with a Gatan K2 Summit direct detector. Automated data collection was carried out using Leginon[70] at a nominal magnification of 36,000x with a pixel size of 1.16 Å. The dose rate was adjusted to 8 counts/pixel/s, and each movie was acquired in counting mode fractionated in 50 frames of 200 ms. 3,138 micrographs were collected in a single session with a defocus range comprised between −0.5 and −3.0 μm. Preprocessing was performed using Warp[71] and particle images were extracted with a box size of 400 pixelŝ2.

For the S/S2D106 and S/S2H97 datasets, two rounds of reference-free 2D classification were performed using CryoSPARC to select well-defined particle images[72]. These selected particles were subjected to two rounds of 3D classification with 50 iterations each (angular sampling 7.5° for 25 iterations and 1.8° with local search for 25 iterations), using our previously reported closed SARS-CoV-2 S structure as initial model[49] (PDB 6VXX) in Relion[73]. 3D refinements were carried out using non-uniform refinement[74] along with per-particle defocus refinement in CryoSPARC. Selected particle images were subjected to the Bayesian polishing procedure[75] implemented in Relion3.0 before performing another round of non-uniform refinement in CryoSPARC followed by per-particle defocus refinement and again non-uniform refinement.

To further improve the density of the S2D106 Fab, the particles were then subjected to focus 3D classification without refining angles and shifts using a soft mask on RBD and Fab variable domains with a tau value of 60 in Relion. Particles belonging to classes with the best resolved local density were selected and subject to local refinement using CryoSPARC. Local resolution estimation, filtering, and sharpening were carried out using CryoSPARC. Reported resolutions are based on the gold-standard Fourier shell correlation (FSC) of 0.143 criterion and Fourier shell correlation curves were corrected for the effects of soft masking by high-resolution noise substitution[76]. UCSF Chimera[77] and Coot[78] were used to fit atomic models into the cryoEM maps. Spike-RBD/S2D106 Fab model was refined and relaxed using Rosetta using sharpened and unsharpened maps[79].

S2H97-induced spike refolding

10 μM native-like SARS-CoV-2 S was incubated with 13 μM S2H97 Fab for 1 hour at room temperature. Samples were diluted to 0.01 mg/mL immediately prior to adsorption to glow-discharged carbon-coated copper grids for ~30 sec prior to a 2% uranyl formate staining. Micrographs were recorded using the Leginon software[70] on a 120 kV FEI Tecnai G2 Spirit with a Gatan Ultrascan 4000 4k × 4k CCD camera at 67,000 nominal magnification. The defocus ranged from −1.0 to −2.0 μm and the pixel size was 1.6 Å.

Cell-surface antibody-mediated S1 shedding

CHO-K1 cells stably expressing the prototypic SARS-CoV-2 spike protein were harvested, washed in wash buffer (PBS + 1% BSA, 2 mM EDTA) and resuspended in PBS. 90,000 cells per well were dispensed into round bottom 96-well plates (Corning), and treated with 10 μg/mL TPCK-Trypsin (Worthington Biochem) for 30 min at 37°C. Cells were washed and incubated with 15 μg/mL antibody across 5, 30, 60, 120, and 180 min timepoints at 37°C. Cells were washed with ice-cold wash buffer, and stained with 1.5 μg/mL Alexa Fluor647-conjugated goat anti-human IgG secondary antibody (Jackson Immunoresearch) for 30 min on ice in the dark. Cells were washed twice with cold wash buffer and analyzed using a ZE5 cytometer (Biorad) with acquisition chamber at 4°C. Binding at each time point was measured as mean fluorescence intensity (MFI), normalized to the MFI at the 5 min labeling time point. Data was analyzed and plotted using GraphPad Prism v. 9.0.1.

Cell-cell fusion of CHO-S cells

Cell-cell fusion between S-expressing CHO-K1 cells was performed as described by Lempp et al.[31]. CHO-K1 cells stably expressing the prototypic SARS-CoV-2 spike protein were seeded in 96-well plates (Thermo Fisher Scientific) at 12,500 cells/well. The following day, antibody and nuclei marker Hoechst (final dilution 1:1000) were added to cells and incubated for 24 h. Cell-cell fusion was visualized using the Cytation 5 Imager (BioTek), and an object detection protocol was used to detect nuclei and measure their size. The nuclei of fused cells (syncytia) are aggregated at the center of the syncytia and recognized as a uniquely large object that is gated according to its size. To quantify cell-cell fusion, we report the area of objects in fused cells divided by the total area of all objects, multiplied by 100 to represent as a percentage.

Antibody blockade of RBD binding to ACE2

ACE2 blockade ELISA was performed as described by Piccoli et al.[15]. Unlabeled antibodies were serially diluted, mixed with RBD mouse Fc-tagged antigen (Sino Biological, final concentration 20 ng/mL) and incubated for 30 min at 37°C. The mix was added for 30 min to ELISA 96-well plates (Corning) pre-coated overnight at 4°C with 2 μg/mL human ACE2 in PBS. Plates were washed and RBD binding was revealed using secondary goat anti-mouse IgG (Southern Biotech 1030–04). After washing, pNPP substrate was added and plates were read at 405 nm. The percentage of inhibition was calculated as: $(1 - (\text{OD sample} - \text{OD neg ctrl})/(\text{OD pos ctrl} - \text{OD neg ctrl})]) \times 100$.

Inhibition of spike-mediated cell-to-cell fusion

Cell-to-cell fusion inhibition assays were performed as described by McCallum et al.[80]. Vero E6 cells were seeded in 96 well plates at 15,000 cells per well in 70 mL DMEM with high glucose and 2.4% FBS (Hyclone). After 16 h at 37°C with 8% CO2, the cells were transfected as follows: for 10 wells, 0.57 mg plasmid SARS-CoV-2-S-D19_pcDNA3.1 was mixed with 1.68 mL X-tremeGENE HP in 30 mL OPTIMEM. After 15 min incubation, the mixture was diluted 1:10 in DMEM medium and 30 mL was added per well. 4-fold antibody serial dilutions were prepared and added to the cells, with a starting concentration of 20 μg/mL. The following day, 30 μL 5X concentrated DRAQ5 in DMEM was added per well and incubated for 2 h at 37°C. Nine images of each well were acquired with a Cytation 5 equipment for analysis.

S2H97 prophylactic protection in Syrian hamsters

We used a validated SARS-CoV-2 Syrian Golden hamster model of infection[81,82] to test S2H97 prophylactic efficacy. Experiments were performed in the high-containment A3 and BSL3+ facilities of the KU Leuven Rega Institute (3CAPS) under licenses AMV 30112018 SBB 219 2018 0892 and AMV 23102017 SBB 219 20170589 according to institutional guidelines.

Syrian hamsters (*Mesocricetus auratus*) were purchased from Janvier Laboratories. Hamsters were housed per two in ventilated isolator cages (IsoCage N Biocontainment System, Tecniplast) with ad libitum access to food, water, and cage enrichment (wood block). Housing conditions and experimental procedures were approved by the ethical committee of animal experimentation of KU Leuven (license P065-2020). Sample sizes of 6 hamsters was determined in order to have a significant difference of at least 1 log viral RNA level (effect size d=2.004) between control and treatment groups, by using a 2-tail t-test with 80% power and an alpha of 0.05, calculated with G*Power 3.1 software. 6–10-week-old female hamsters were randomized for administration of 25 mg/kg S2H97 antibody or 20 mg/kg human isotype control via intraperitoneal injection. Approximately 5 h before infection, animals were anesthetized with isoflurane to allow collection of a blood sample from the jugular vein to be used for antibody quantification. Forty-eight hours post antibody injection, hamsters were infected intranasally with 1.89×10^6 $TCID_{50}$ SARS-CoV-2 virus in 50 µL inoculum. The challenge virus was a SARS-CoV-2 Wuhan isolate from February, 2020 (EPI_ISL_407976), passaged on Vero E6 cells. Passage 6 stock titer was determined by end-point dilution on Vero E6 cells by the Reed and Muench method[83], expressed as 50% tissue culture infectious dose ($TCID_{50}$).

Hamsters were monitored for appearance, behavior, and weight. At day 4 post-infection, hamsters were euthanized by intraperitoneal injection of 500 µL Dolethal (200 mg/mL sodium pentobarbital, Vétoquinol SA). Lungs were collected, homogenized via bead disruption (Precellys) in 350 µL RLT buffer (RNeasy Mini kit, Qiagen) and centrifuged (10,000 rpm, 5 min, 4°C) to pellet cell debris. RNA was extracted using a NucleoSpin kit (Macherey-Nagel) according to manufacturer instructions. RT-qPCR was performed on a LightCycler96 platform (Roche) using the iTaq Universal Probes One-Step RT-qPCR kit (BioRad) with N2 primers and probes targeting the nucleocapsid[81]. Standards of SARS-CoV-2 cDNA (IDT) were used to express viral genome copies per mg tissue. To quantify infectious SARS-CoV-2 particles, endpoint titrations were performed on confluent Vero E6 cells in 96-well plates. Viral titers were calculated as above, and were expressed as $TCID_{50}$ per mg tissue. The circulating antibody levels were measured by Mesoscale bridging ELISA, using an anti-human LS mutation mAb as a capture and anti-human CH2 mAb as detection. Technicians performing RNA, virus, and antibody quantification were blinded to the treatment groups of processed samples. RNA and viral levels were compared between treatment and control via 2-tailed Mann-Whitney test, excluding the two treatment animals with undetectable S2H97 levels at time of viral challenge.

Blockade of binding serology competition assays

Sera blockade of antibody binding was performed as described in Piccoli et al.[15]. Briefly, human IgG1 antibodies were biotinylated using the EZ-link NHS-PEO solid phase biotinylation kit (Pierce). Each labeled antibody was tested for binding to RBD by ELISA, and a concentration for each antibody competition experiment was selected to achieve 80% maximal binding (EC_{80}). ELISA 96-well plates (Corning) were pre-coated overnight at 4°C with 1 µg/mL of mouse Fc-tagged RBD antigen (Sino Biological) in PBS. Unlabeled sera/plasma were serially diluted and added to ELISA plates for 30 min, followed by addition of biotinylated anti-RBD antibody at its EC_{80} concentration. After 30 min incubation, plates were washed and antibody binding was detected using alkaline phosphatase-conjugated streptavidin (Jackson ImmunoResearch). Plates were washed, pNPP substrate (Sigma-Aldrich) was added, and plates were read at 405 nm. The percentage of inhibition of antibody binding was calculated as: $(1–(OD_{sample} - OD_{neg\ ctrl}) / (OD_{pos\ ctrl} - OD_{neg\ ctrl}) \times 100$.

Selection of VSV-SARS-CoV-2 monoclonal antibody resistance mutants (MARMS)

VSV-SARS-CoV-2 S chimera was used to select for SARS-CoV-2 S monoclonal antibody resistant mutants (MARMS) as previously described[1,84]. Briefly, MARMS were recovered by plaque isolation on Vero E6 cells (ATCC, CRL-1586) with the indicated mAb in the overlay. The concentration of mAb in the overlay was determined by neutralization assays at a multiplicity of infection (MOI) of 100. Escape clones were plaque-purified on Vero cells (ATCC, CCL-81) in the presence of mAb, and plaques in agarose plugs were amplified on MA104 cells (Gift from Harry Greenberg) with the mAb present in the medium. Viral stocks were amplified on MA104 cells at an MOI of 0.01 in Medium 199 containing 2% FBS and 20 mM HEPES pH 7.7 (Millipore Sigma) at 34°C. Viral supernatants were harvested upon extensive cytopathic effect and clarified of cell debris by centrifugation at 1,000 × g for 5 min. Aliquots were maintained at −80°C. Viral RNA was extracted from VSV-SARS-CoV-2 mutant viruses using RNeasy Mini kit (Qiagen), and S was amplified using OneStep RT-PCR Kit (Qiagen). The mutations were identified by Sanger sequencing (GENEWIZ). Their resistance was verified by subsequent virus infection in the presence or absence of antibody. Briefly, Vero cells were seeded into 12 well plates for overnight. The virus was serially diluted using DMEM and cells were infected at 37°C for 1 h. Cells were cultured with an agarose overlay in the presence or absence of mAb at 34°C for 2 days. Plates were scanned on a biomolecular imager and expression of eGFP is shown at 48 h post-infection. The S2X58-selected mutation S494L is not shown in Fig. 3a, as its effect on RBD expression was below the deep mutational scanning computational filter.

Viral replication fitness assays

Vero E6 cells (ATCC, CRL-1586) were seeded at 1×10^6 cells per well in 6-well plates. Cells were infected with multiplicity of infection (MOI) of 0.02, with WT and four mutant VSV-SARS-CoV-2 S chimeras mixed at equal (0.20) frequencies. Following 1 h incubation, cell monolayers were washed three times with HBBS and cultures were incubated for 72 h in humidified incubators at 34°C. To passage the progeny viruses, virus mixture was continuously passaged four times in Vero E6 cells at MOI of 0.02. Cellular RNA samples from each passages were extracted using RNeasy Mini kit (QIAGEN) and subjected to next-generation sequencing as described previously to confirm the introduction and frequency of substitutions[84].

Molecular dynamics simulations

Full details of molecular dynamics workflow and analysis are available on GitHub: https://github.com/choderalab/rbd-ab-contact-analysis. The RBD:S309 complex was constructed from PDB ID 7JX3 (Chains A, B, and R). 7JX3 was first refined using ISOLDE[67]. Refinement included adjusting several rotamers, flipping several peptide bonds, fixing several weakly resolved waters, and building in a missing four-residue-long loop. Though the N343 glycan N-Acetylglucosamine (NAG) was present in 7JX3, ISOLDE was used to construct a complex glycan at N343. The full glycosylation pattern was determined from Shajahan et al.[85] and Watanabe et al.[86]. The glycan structure used for N343 (FA2G2) corresponds to the most stable conformer obtained from multi microsecond molecular dynamics (MD) simulations of cumulative sampling[87]. The base NAG residue in FA2G2 was aligned to the corresponding NAG stub in the RBD:S309 model and any resulting clashes were refined in ISOLDE. The same process was repeated for the RBD:S2H97 crystal structure.

The refined glycosylated RBD:S309 and RBD:S2H97 complexes were prepared for simulation using tleap from AmberTools20[88]. All relevant disulfide bridges and covalent connections in glycan structures were specified. The glycosylated proteins were parameterized with the Amber ff14SB[89] and GLYCAM_06j-1[90] force fields. The systems were solvated using the TIP3P rigid water model[91] in a truncated octahedral box with 2.2 nm solvent padding on all sides. The solvent box's shape and size were chosen to prevent the protein complex from interacting with its periodic image. The solvated systems were then neutralized with 0.15 M NaCl using the Li/Merz ion parameters of monovalent ions for the TIP3P water model (12–6 normal usage set)[92]. Virtual bonds were added across chains that should be imaged together to aid the post-processing of trajectories.

Each system was energy-minimized with an energy tolerance of 10 kJ mol^{-1} and equilibrated five times independently using the OpenMMTools 0.20.0 (https://github.com/choderalab/openmmtools) BAOAB Langevin integrator[93] for 20 ns in the NPT (p=1 atm, T = 310 K) ensemble with a timestep of 4.0 femtoseconds, a collision rate of 1.0 picoseconds^{-1}, and a relative constraint tolerance of 1×10^{-5}. Hydrogen atom masses were set to 4.0 amu by transferring mass from connected heavy atoms, bonds to hydrogen were constrained, and center of mass motion was not removed. Pressure was controlled by a molecular-scaling Monte Carlo barostat with an update interval of 25 steps. Non-bonded interactions were treated with the Particle Mesh Ewald method[94] using a real-space cutoff of 1.0 nm and the OpenMM default relative error tolerance of 0.0005, with grid spacing selected automatically. The simulations were subsequently packaged to seed for production simulation on Folding@home[95,96]. Default parameters were used unless noted otherwise.

The equilibrated structures (five per complex) were used to initiate parallel distributed MD simulations on Folding@home[95,96]. Simulations were run with OpenMM 7.4.2 (compiled into Folding@home core22 0.0.13). Production simulations used the same Langevin integrator as the NPT equilibration described above. 5000 and 4985 independent MD simulations were generated on Folding@home for RBD:S309 and RBD:S2H97, respectively. Conformational snapshots (frames) were stored at an interval of 1 ns/frame for subsequent analysis. The final datasets contained 1.1 ms and 623.7 μs of aggregate simulation time for RBD:S309 and RBD:S2H97, respectively. This trajectory dataset (without solvent) are available at the MolSSI COVID-19 Molecular Structure and Therapeutics Hub: https://covid.molssi.org//simulations/#foldinghome-simulations-of-the-sars-cov-2-spike-rbd-bound-to-monoclonal-antibody-s309 and https://covid.molssi.org//simulations/#foldinghome-simulations-of-the-sars-cov-2-spike-rbd-bound-to-monoclonal-antibody-s2h97.

The first 100 ns of each trajectory was discarded (to allow relaxation away from the crystal structure), yielding total simulation times of 644.3 and 262.9 μs used for analysis of RBD:S309 and RBD:S2H97 systems, respectively. All trajectories had solute structures aligned to their first frame and centered using MDTraj[97]. Residues were considered to be at the interface if they were within 10 Å of any antibody Fab / RBD residue (with the exception of RBD N343 glycans, where all glycan residues were considered). The minimum distance of heavy atoms between every pair of interface residues was computed for every frame (1 ns) using MDAnalysis[98,99]. A close contact was counted if the minimum distance between a residue pair was below 3.5 Å (if one of the residues was hydrophobic, a 4.5 Å cutoff was used). The contribution of each RBD residue to close contacts was calculated as a percentage by summation of the number of close contacts for a particular RBD residue and normalizing by the total number of close contact interactions over all frames of each simulation.

Materials Availability

- The SARS-CoV-2 RBD mutant libraries (#1000000172) and unmutated parental plasmid (#166782) are available on Addgene
- Other materials generated in this study will be made available on request and may require a material transfer agreement

Data Availability

- Interactive escape maps and structural visualizations can be found at: https://jbloomlab.github.io/SARS-CoV-2-RBD_MAP_Vir_mAbs/
- Raw Illumina sequencing data from deep mutational scanning experiments are available on NCBI SRA, BioSample SAMN18315604 (SARS-CoV-2 mutant selection data) and BioSample SAMN18316011 (sarbecovirus RBD selection data).
- PacBio sequencing data used to link N16 barcodes to sarbecovirus RBD variant are available on NCBI SRA, BioSample SAMN18316101.
- Complete table of deep mutational scanning antibody escape fractions is provided on GitHub: https://github.com/jbloomlab/SARS-CoV-2-RBD_MAP_Vir_mAbs/blob/main/results/supp_data/all_antibodies_raw_data.csv. This table includes both antibodies first described in this study (Fig. 1b,c), and all other antibody selections that were re-processed to generate Fig. 4a.
- The X-ray structure data and model has been deposited with accession code PDB 7R6W for RBD-S2X35-S309, PDB 7M7W for RBD-S2H97-S2X259 and PDB 7R6X for RBD-S2E12-S304-S309.
- CryoEM structure data and model are available with accession codes EMD-24300 for S/S2D106, EMD-24299 and PDB 7R7N for the S/S2D106 local refinement, and EMD-24301 for S/S2H97
- The raw and processed molecular dynamics trajectory data are available at the MolSSI COVID-19 Molecular Structure and Therapeutics Hub: https://covid.molssi.org//simulations/#foldinghome-simulations-of-the-sars-cov-2-spike-rbd-bound-to-monoclonal-antibody-s309 and https://covid.molssi.org//simulations/#foldinghome-simulations-of-the-sars-cov-2-spike-rbd-bound-to-monoclonal-antibody-s2h97
- All other datasets generated during and/or analyzed during the current study are available from the corresponding author on reasonable request

Code Availability

- Repository containing all code, analysis, and summary notebooks for the analysis of the SARS-CoV-2 deep mutational scanning escape selections available on GitHub: https://github.com/jbloomlab/SARS-CoV-2-RBD_MAP_Vir_mAbs
- Repository containing code and analysis of the sarbecovirus RBD library binding experiments available on GitHub: https://github.com/jbloomlab/SARSr-CoV_RBD_MAP
- Repository containing code and analysis of molecular dynamics simulations is available on GitHub: https://github.com/choderalab/rbd-ab-contact-analysis

Extended Data

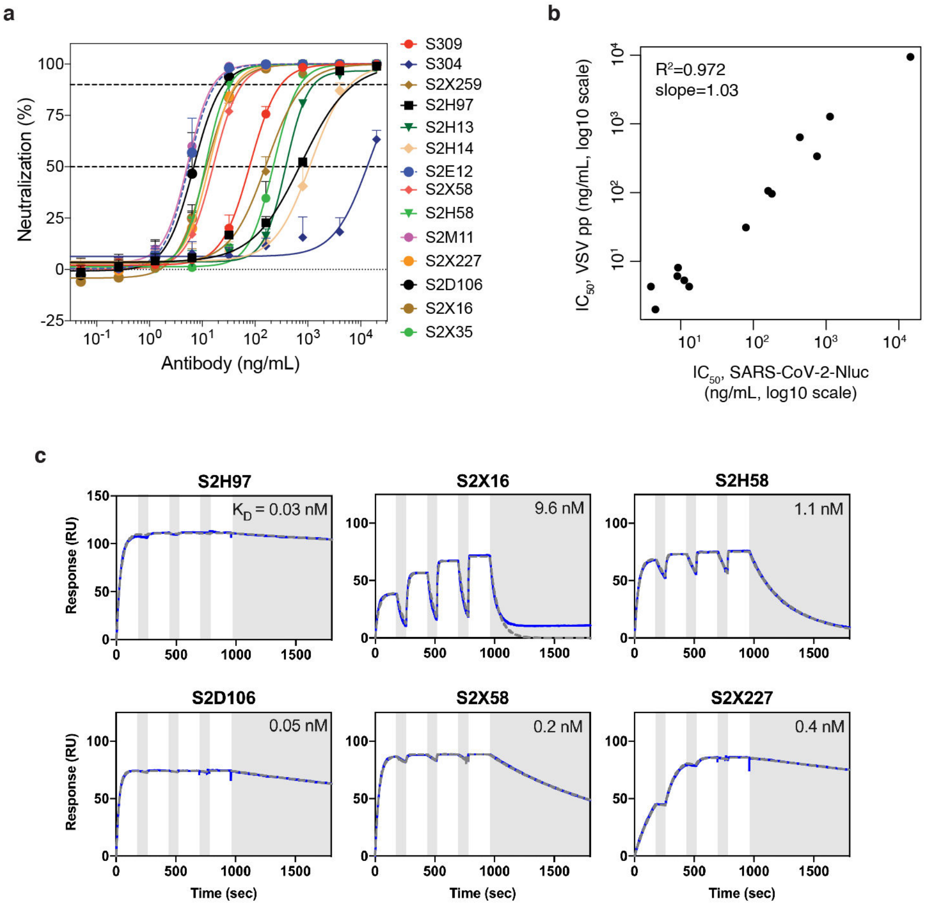

d

		NTD	RBD	S1/S2	S2
B.1.351	South Africa	L18F/D80A/D215G/R246I/242-244 del	K417N/E484K/N501Y	D614G	A701V
B.1.1.7	UK	H69-/ V70-/ Y144-	N501Y	A570D/D614G/P681H	T716I/S982A/D1118H
P.1	Brazil	L18F/T20N/P26S/D138Y/R190S	K417T/E484K/N501Y	D614G/H655Y	T1027I/V1167F
B.1.429	California	S13I/W152C	L452R	D614G	
B.1.1.519	Mexico-Swiss		T478K	D614G/P681H	T732A
B.1.526	New York	L5F/T95I/D253G	E484K	D614G	A701V
B.1.258	UK (Scotland)	H69-/ V70-	N439K	D614G	
B.1.525	Nigeria	Q52R/A67V/H69-/V70-/Y144-	E484K	D614G/Q677H	F888L
R.1		W152L	E484K	D614G	G769V
R.2			E484K	D614G/Q677H	T732S/E1202Q
B.1.1.7+E484K	UK (Bristol)	H69-/ V70-/ Y144-	E484K/N501Y	A570D/D614G/P681H	T716I/S982A/D1118H
B.1.1.7 + S494P	UK	H69-/ V70-/ Y144-	N501Y/S494P	A570D/D614G/P681H	T716I/S982A/D1118H
A.23.1	UK (Liverpool)	R102I/F157L	V367F/E484K	Q613H/P681R	

Extended Data Fig. 1. Antibody neutralization and binding data.

a, Neutralization of authentic SARS-CoV-2 (SARS-CoV-2-Nluc) by 14 antibodies. Shown are representative live virus neutralization plots, measured with entry into Vero E6 cells. Symbols are means ± SD of technical triplicates. Dashed lines indicate IC_{50} and IC_{90} values. All antibodies were measured at each concentration point in the series, with hidden points due to overplotting reflecting overlap at the upper and lower neutralization limits. **b**, Correlation in antibody neutralization IC_{50} as determined in spike-pseudotyped VSV particles (n = 3 to 8) versus authentic SARS-CoV-2 (n = 3). **c**, Representative SPR sensorgrams of Fab fragments of the six newly described antibodies binding to the SARS-CoV-2 RBD. White and gray stripes indicate association and dissociation phases, respectively. Binding affinities for previously described antibodies shown in Fig. 1a are consistent with measurements from Piccoli et al. (S304, S309, S2X35, S2H13, S2H14)[15] and Tortorici et al. (S2E12)[8]. **d**, Identifiers and spike genotypes of SARS-CoV-2 variants tested in neutralization assays in Figs. 2d and 3b.

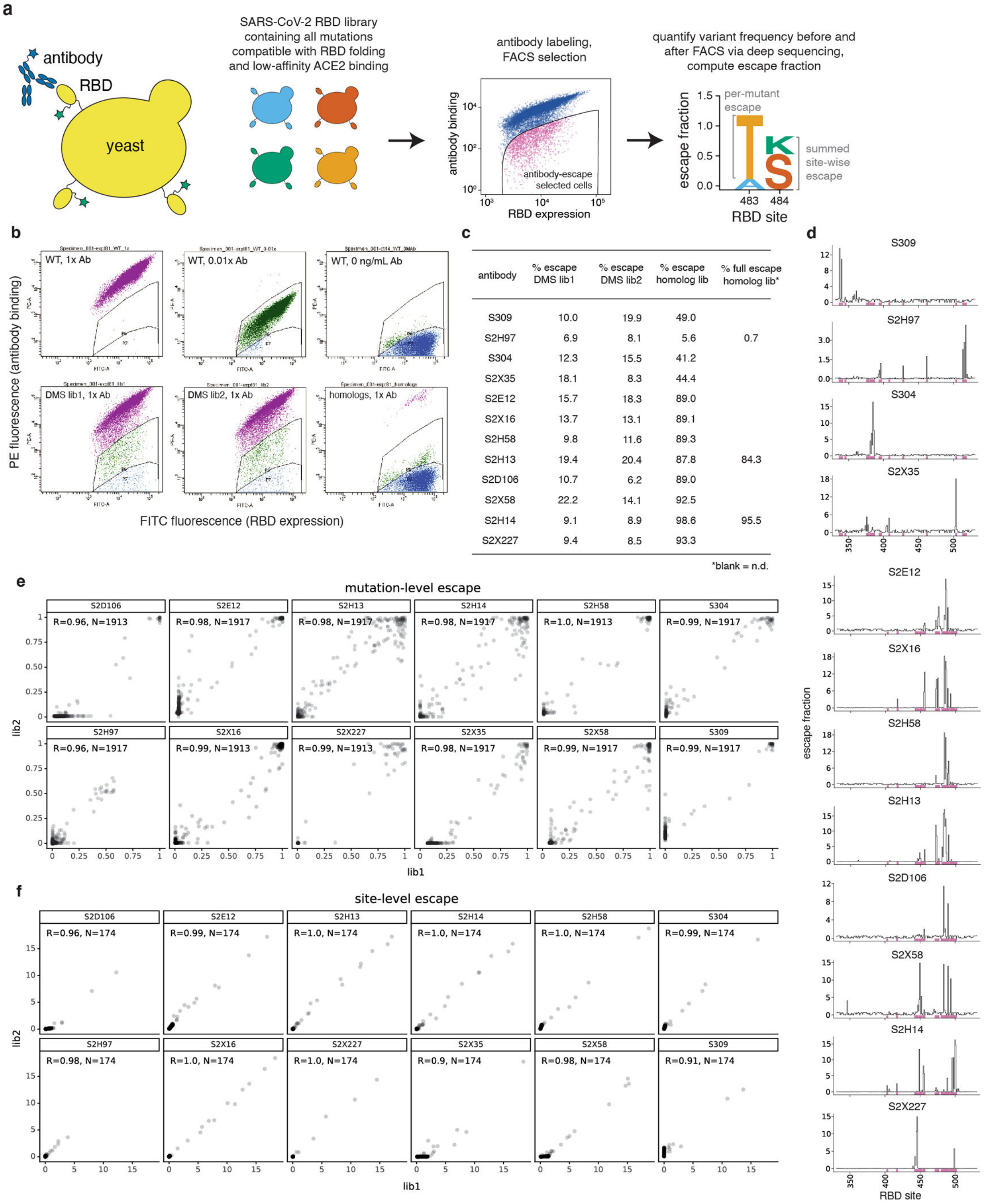

antibody	% escape DMS lib1	% escape DMS lib2	% escape homolog lib	% full escape homolog lib*
S309	10.0	19.9	49.0	
S2H97	6.9	8.1	5.6	0.7
S304	12.3	15.5	41.2	
S2X35	18.1	8.3	44.4	
S2E12	15.7	18.3	89.0	
S2X16	13.7	13.1	89.1	
S2H58	9.8	11.6	89.3	
S2H13	19.4	20.4	87.8	84.3
S2D106	10.7	6.2	89.0	
S2X58	22.2	14.1	92.5	
S2H14	9.1	8.9	98.6	95.5
S2X227	9.4	8.5	93.3	

*blank = n.d.

Extended Data Fig. 2. Deep mutational scanning to map mutations that escape antibody binding.

a, Scheme of the deep mutational scanning assay. Conformationally intact RBD is expressed on the surface of yeast, where RBD expression and antibody binding is detectable via fluorescent labeling. We previously constructed mutant libraries containing virtually all of the 3,819 possible amino acid mutations in the SARS-CoV-2 RBD[26] and sorted the library to eliminate mutations that destabilize the RBD or strongly reduce ACE2-binding affinity[3]. We incubate the library with a sub-saturating antibody concentration and use fluorescence-activated cell sorting (FACS) to isolate yeast cells expressing RBD mutants with reduced antibody binding. Deep sequencing quantifies mutant frequencies before and after FACS selection, enabling calculation of the “escape fraction” of each amino acid mutation, which reflects the fraction of cells carrying that mutation that fall into the antibody-escape bin. Mutation escape fractions are represented in logoplots, where the height of a letter reflects the extent of escape from antibody binding. **b**, Representative selection gates, after gating for single cells expressing RBD as in Greaney et al.[3]. Yeast expressing the SARS-CoV-2 RBD (top panels) are labeled at 1x, 0.01x and no antibody to guide selection gates. Mutant RBDs that reduce binding (green, gate drawn to capture 0.01x WT control) are sorted and sequenced for calculation of mutant escape fractions. This same gate was used to quantify escape within libraries of yeast expressing all sarbecovirus RBD homologs. For several antibodies, we also selected the sarbecovirus RBD library with a more stringent “full escape” gate (blue, gate drawn to capture 0 ng/mL WT control). **c**, Fraction of library cells falling into escape bins for each antibody selection. **d**, Line plots showing total escape at all RBD sites for each antibody. Sites of strong escape illustrated in logoplots in Fig. 1b,c shown with pink indicators. **e**,**f**, Correlation in per-mutation (**e**) and per-site (**f**, sum of per-mutation) escape fractions for duplicate libraries that were independently generated and assayed. *N*, number of mutations (**e**) or sites (**f**) in the correlation.

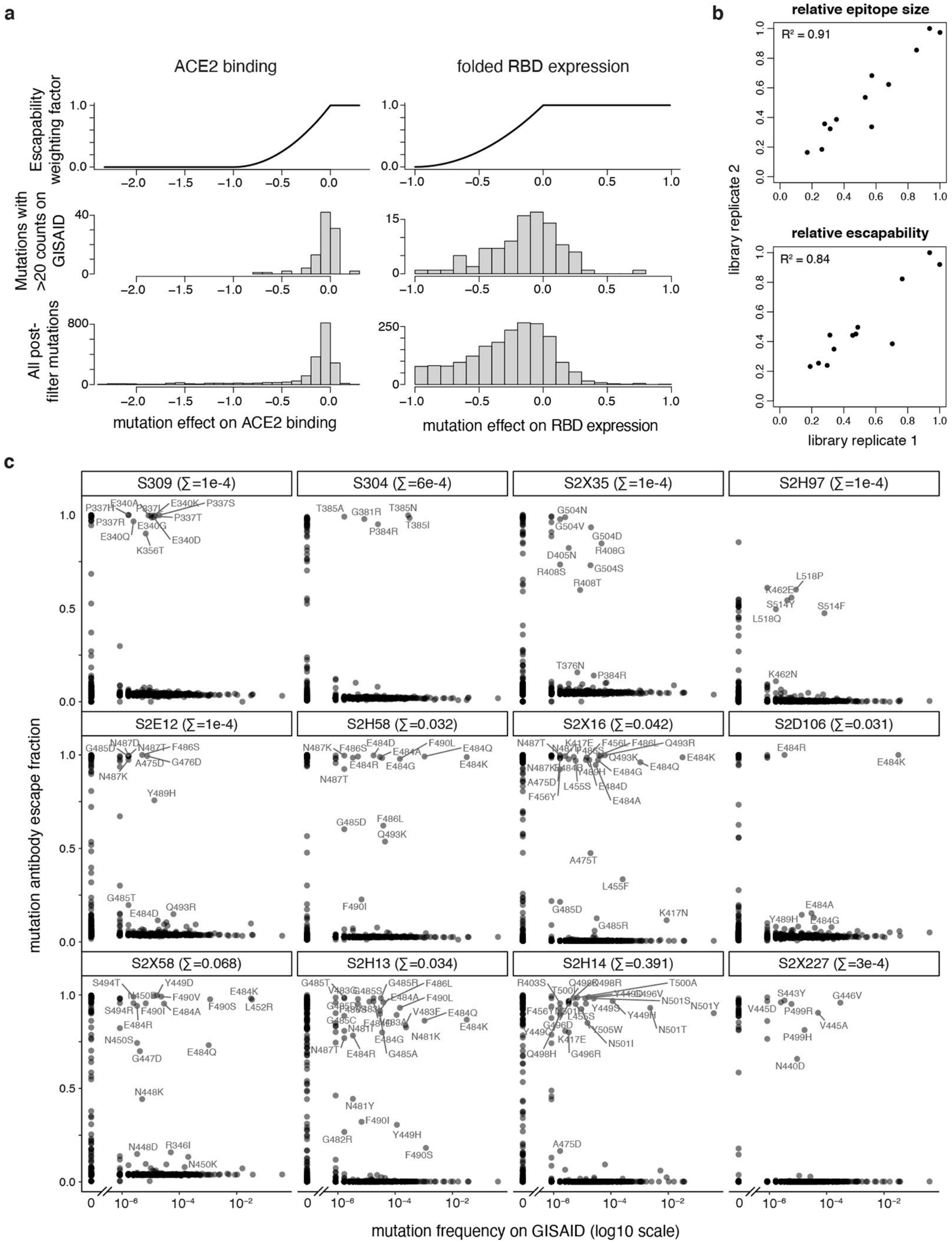

Extended Data Fig. 3. Antibody escapability from deep mutational scanning measurements and in natural SARS-CoV-2 mutants.

a, To calculate antibody escapability (Fig. 1b,c), mutation escape fractions were weighted by their deleterious consequences for ACE2 binding or RBD expression. Top plots show the weighting factor (y-axis) for mutation effects on ACE2 binding (left) and RBD expression (right). This weight factor was multiplied by the mutation escape fraction in the summation to calculate antibody escapability as described in the Methods. Histograms show the distribution of mutation effects on ACE2 binding (left) and RBD expression (right) for all mutations that pass our computational filtering steps (bottom), and mutations that are found with at least 20 sequence counts on GISAID (middle). **b**, Correlation in antibody relative epitope size (top) and escapability (bottom) calculated from independent deep mutational scanning replicates, compared to the averaged replicates shown in Fig. 1b,c. R^2, squared Pearson correlation coefficient. **c**, Scatterplots illustrate the degree to which a mutation escapes antibody binding (escape fraction, y-axis) and its frequency among 1,190,241 high-quality human-derived SARS-CoV-2 sequences present on GISAID as of May 2, 2021. Large escape mutations (>5x global median escape fraction) for each antibody with non-zero mutant frequencies are labeled. Plot labels report the sum of mutant frequencies for all labeled mutations, corresponding to the natural SARS-CoV-2 mutant escape frequency for antibodies shown in Fig. 4d,g.

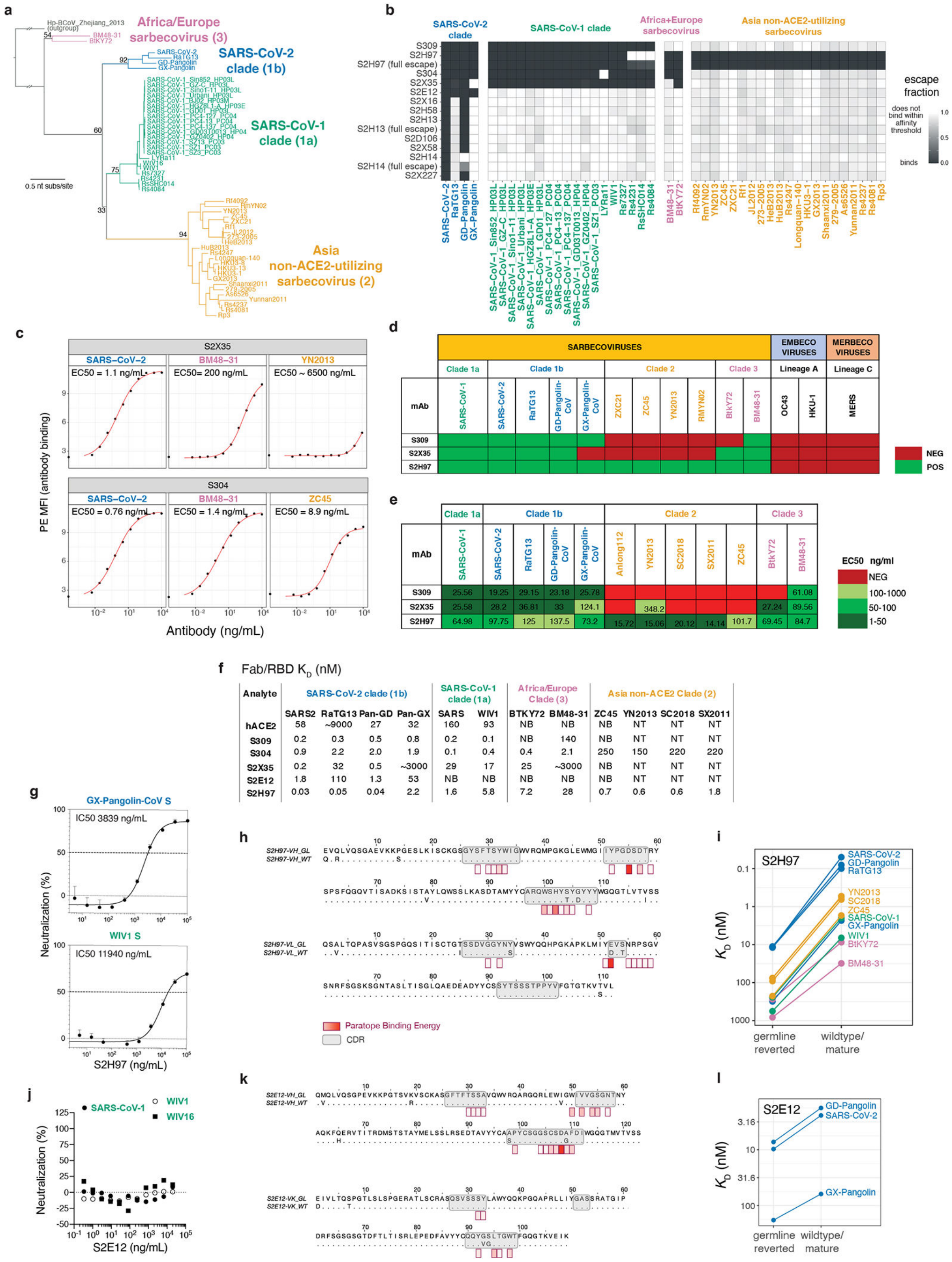

d

	SARBECOVIRUSES											EMBECO VIRUSES		MERBECO VIRUSES
	Clade 1a	Clade 1b				Clade 2				Clade 3		Lineage A		Lineage C
mAb	SARS-CoV-1	SARS-CoV-2	RaTG13	GD-Pangolin-CoV	GX-Pangolin-CoV	ZXC21	ZC45	YN2013	RMYN02	BtKY72	BM48-31	OC43	HKU-1	MERS
S309	🟩	🟩	🟩	🟩	🟩	🟥	🟥	🟥	🟥	🟥	🟩	🟥	🟥	🟥
S2X35	🟩	🟩	🟩	🟩	🟥	🟥	🟥	🟥	🟥	🟩	🟩	🟥	🟥	🟥
S2H97	🟩	🟩	🟩	🟩	🟩	🟩	🟩	🟩	🟩	🟩	🟩	🟥	🟥	🟥

🟥 NEG
🟩 POS

e

	Clade 1a	Clade 1b				Clade 2					Clade 3	
mAb	SARS-CoV-1	SARS-CoV-2	RaTG13	GD-Pangolin-CoV	GX-Pangolin-CoV	Anlong112	YN2013	SC2018	SX2011	ZC45	BtKY72	BM48-31
S309	25.56	19.25	29.15	23.18	25.78	🟥	🟥	🟥	🟥	🟥	🟥	61.08
S2X35	25.58	28.2	36.81	33	124.1	🟥	348.2	🟥	🟥	🟥	27.24	89.56
S2H97	64.98	97.75	125	137.5	73.2	15.72	15.06	20.12	14.14	101.7	69.45	84.7

EC50 ng/ml
🟥 NEG
100-1000
50-100
1-50

f Fab/RBD K_D (nM)

Analyte	SARS-CoV-2 clade (1b)				SARS-CoV-1 clade (1a)		Africa/Europe Clade (3)		Asia non-ACE2 Clade (2)			
	SARS2	RaTG13	Pan-GD	Pan-GX	SARS	WIV1	BTKY72	BM48-31	ZC45	YN2013	SC2018	SX2011
hACE2	58	~9000	27	32	160	93	NB	NB	NB	NT	NT	NT
S309	0.2	0.3	0.5	0.8	0.2	0.1	NB	140	NB	NT	NT	NT
S304	0.9	2.2	2.0	1.9	0.1	0.4	0.4	2.1	250	150	220	220
S2X35	0.2	32	0.5	~3000	29	17	25	~3000	NB	NT	NT	NT
S2E12	1.8	110	1.3	53	NB	NB	NB	NB	NB	NT	NT	NT
S2H97	0.03	0.05	0.04	2.2	1.6	5.8	7.2	28	0.7	0.6	0.6	1.8

Extended Data Fig. 4. Breadth of antibody binding across sarbecoviruses.

a, Phylogenetic relationship of sarbecovirus RBDs inferred from aligned nucleotide sequences, with the four sarbecovirus clades labeled in separate colors used throughout the text. Node support values are bootstrap support values. **b**, Breadth of sarbecovirus binding by each antibody to a panel of yeast-displayed sarbecovirus RBDs. Data as in Fig. 1d, with the addition of secondary "full escape" selection data for S2H97, S2H13, and S2H14 (0 ng/mL WT control, Extended Data Fig. 2b,c), enabling differentiation of RBDs with intermediate binding (e.g., S2H97/RsSHC014) versus complete loss of binding. Escape fractions are calculated as the mean of replicate barcoded genotypes internal to the library. Median number of barcodes per RBD is 249, with a range of 104 to 566. The median SEM across escape fraction measurements is 0.019, with a range of 0.00005 to 0.038 across all RBD/antibody pairs. **c**, Flow cytometry detection of antibody binding to isogenic yeast-displayed RBD variants. **d**, Flow cytometry detection of antibody binding to mammalian-surface displayed spikes. **e**, ELISA binding of antibody to purified RBD proteins. **f**, SPR measurement of binding of cross-reactive antibodies (Fab) and human ACE2 to select sarbecovirus RBDs. NB, no binding; NT, not tested. Values from single replicates. **g**, S2H97 neutralization of VSV pseudotyped with select sarbecovirus spikes, with entry measured in ACE2-transduced BHK-21 cells. Curves are representative of two independent experiments. Points represent means, error bars standard deviation from three technical replicates, and IC50 geometric mean of experiments. IC50 values are not comparable to other experiments on Vero E6 cells (e.g. Fig. 2c) due to ACE2 overexpression and its impact on S2H97 neutralization. **h**, Alignment of germline-reverted and mature S2H97 heavy- (top) and light-chain (bottom) amino acid sequences. CDR sequences shown in grey box. Heatmap overlay indicates the predicted energetic contribution of antibody paratope residues from the crystal structure. **i**, Binding of germline-reverted and mature S2H97 to select sarbecovirus RBDs as measured by SPR. **j**, Neutralization of select sarbecoviruses by S2E12 (spike-pseudotyped VSV on 293T-ACE2 cells). Details as in Fig. 3c. **k**, Alignment of germline-reverted and mature S2E12. Details as in (**h**). **l**, Binding of germline-reverted and mature S2E12 to select sarbecovirus RBDs as measured by SPR.

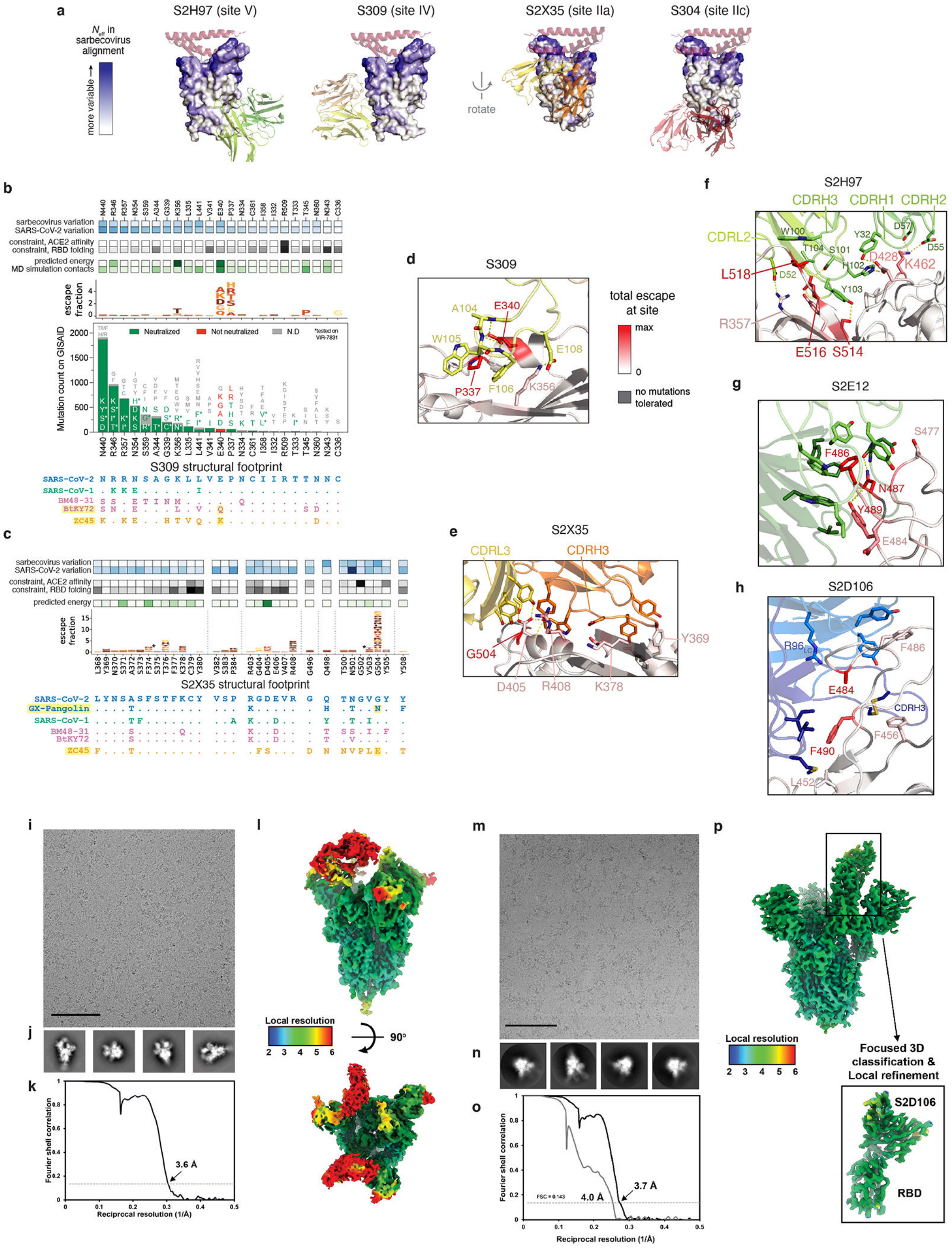

Extended Data Fig. 5. Structures and epitopes of Fab:RBD complexes.

a, Surfaces targeted by broadly binding RBD antibodies. RBD surface is colored by site variability across sarbecoviruses. ACE2 key motifs shown in transparent red cartoon. Antibody variable domains shown as cartoon, with darker shade indicating the heavy chain. **b**,**c**, Integrative features of the S309 (**b**) and S2X35 (**c**) structural epitopes. Details as in Fig. 3g,h and Fig. 2b. **d-h,** Zoomed in view of the RBD bound to S309 (**d**), S2X35 (**e**), S2H97 (**f**), S2E12 (**g**), and S2D106 (**h**), with important contact and escape residues labeled. RBD residues colored by total site escape [scale bar, right of (**d**)]. **i,j**, Representative electron micrograph and 2D class averages of SARS-CoV-2 S in complex with the S2H97 Fab embedded in vitreous ice. Scale bar: 400 Å. Micrographs representative of 3138 micrographs. **k**, Gold-standard Fourier shell correlation curve for the S2H97-bound SARS-CoV-2 S trimer reconstruction. The 0.143 cutoff is indicated by a horizontal dashed line. **l**, Local resolution map calculated using cryoSPARC for the whole reconstruction with two orthogonal orientations. **m,n**, Representative electron micrograph and 2D class averages of SARS-CoV-2 S in complex with the S2D106 Fab embedded in vitreous ice. Scale bar: 400 Å. Micrographs representative of 2166 micrographs **o**, Gold-standard Fourier shell correlation curves for the S2D106-bound SARS-CoV-2 S trimer (black line) and locally refined RBD/S2D106 variable domains (gray line). The 0.143 cutoff is indicated by a horizontal dashed line. **p**, Local resolution map calculated using cryoSPARC for the whole reconstruction and the locally refined RBD/S2D106 variable domain region.

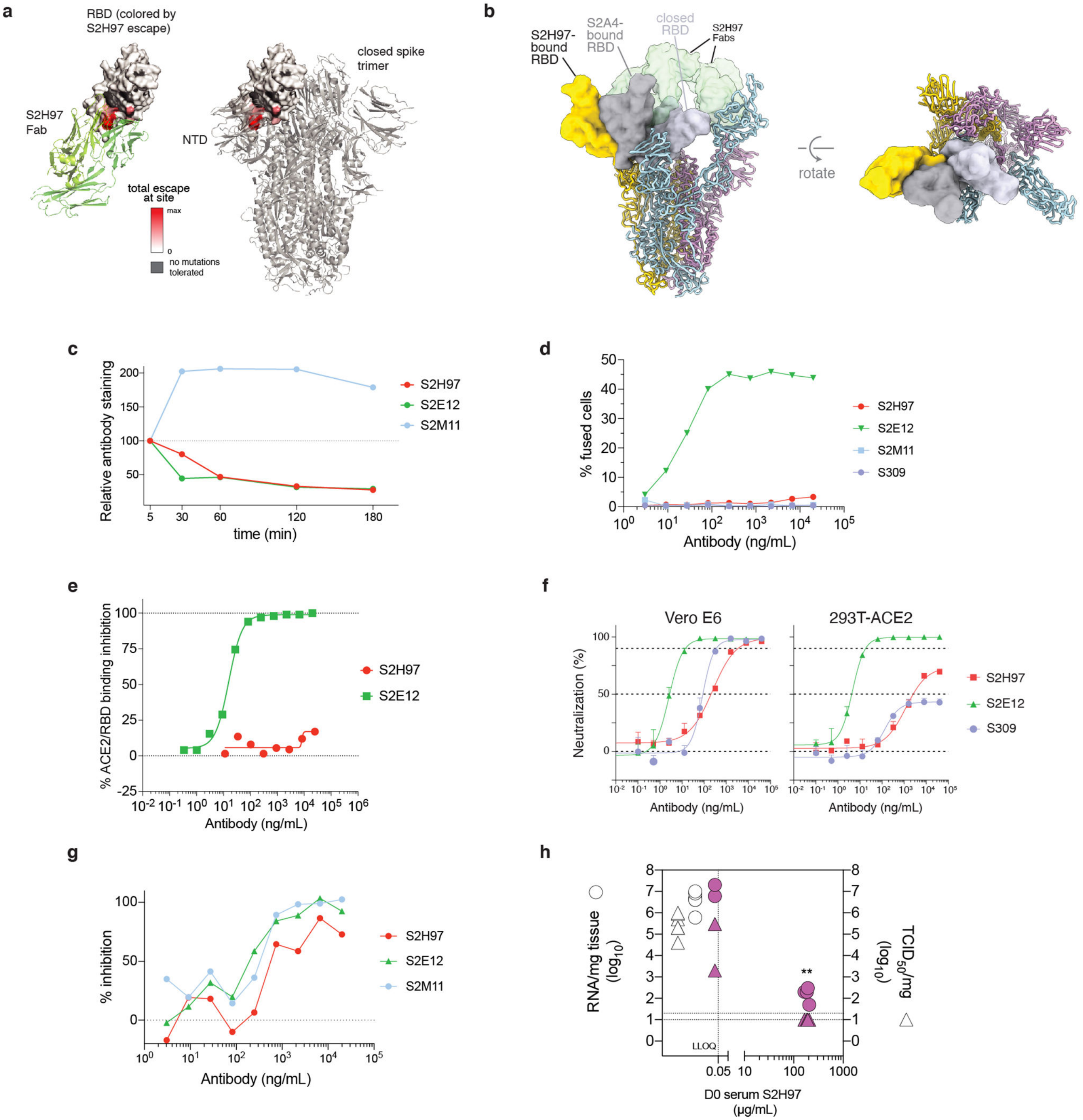

Extended Data Fig. 6. Mechanism of action of S2H97 neutralization and protection.

a, Quaternary context of the S2H97 epitope. Left, S2H97-bound RBD, with RBD sites colored by S2H97 escape (scale bar, bottom). Right, RBD in the same angle as left, in the closed spike trimer. **b**, CryoEM structure of S2H97 Fabs (green surfaces) bound to SARS-CoV-2 S indicating the extensive opening of the RBD (yellow surface) necessary to access the S2H97 epitope. Closed RBD (light purple surface, PDB 7K43) and site II Fab S2A4 bound open RBD (gray surface, PDB 7JVC) are shown for comparison. Spike protomers are shown in yellow, blue, and pink. **c**, Antibody-mediated S_1 shedding from cell-surface expressed SARS-CoV-2 S as determined by flow cytometry. **d**, Cell-cell fusion of CHO cells expressing SARS-CoV-2 S (CHO-S) incubated with variable concentrations of antibody. **e**, Antibody competition with RBD-ACE2 binding determined by ELISA. Points represent mean of technical duplicates. **f**, S2H97 neutralization of SARS-CoV-2 S pseudotyped VSV on ACE2-overexpressing cells (293T-ACE2) compared to Vero E6 cells. Points reflect mean and error bars reflect standard deviation from triplicate measurements. Curves are representative of two biological replicates. **g**, Antibody inhibition of cell-to-cell fusion of Vero E6 cells transfected with SARS-CoV-2 S. **h**, Influence of circulating S2H97 level on prophylactic efficacy in Syrian hamsters. Infectious virus titers (right y-axis, triangles) and RNA levels (left y-axis, circles) reflect the data represented in Fig. 2f, measured in hamsters four days after SARS-CoV-2 challenge in animals prophylactically dosed with 25 mg/kg S2H97 (magenta symbols) or isotype control (white symbols). The levels of circulating S2H97 (D0, before infection, μg/mL) are shown on the x-axis (LLOQ, lower level of quantification). ** p=0.0048 (virus titer) and p=0.0048 (RNA) vs control isotype, two-sided Mann-Whitney test (the 2 animals shown with no detectable serum antibody were excluded from the comparison).

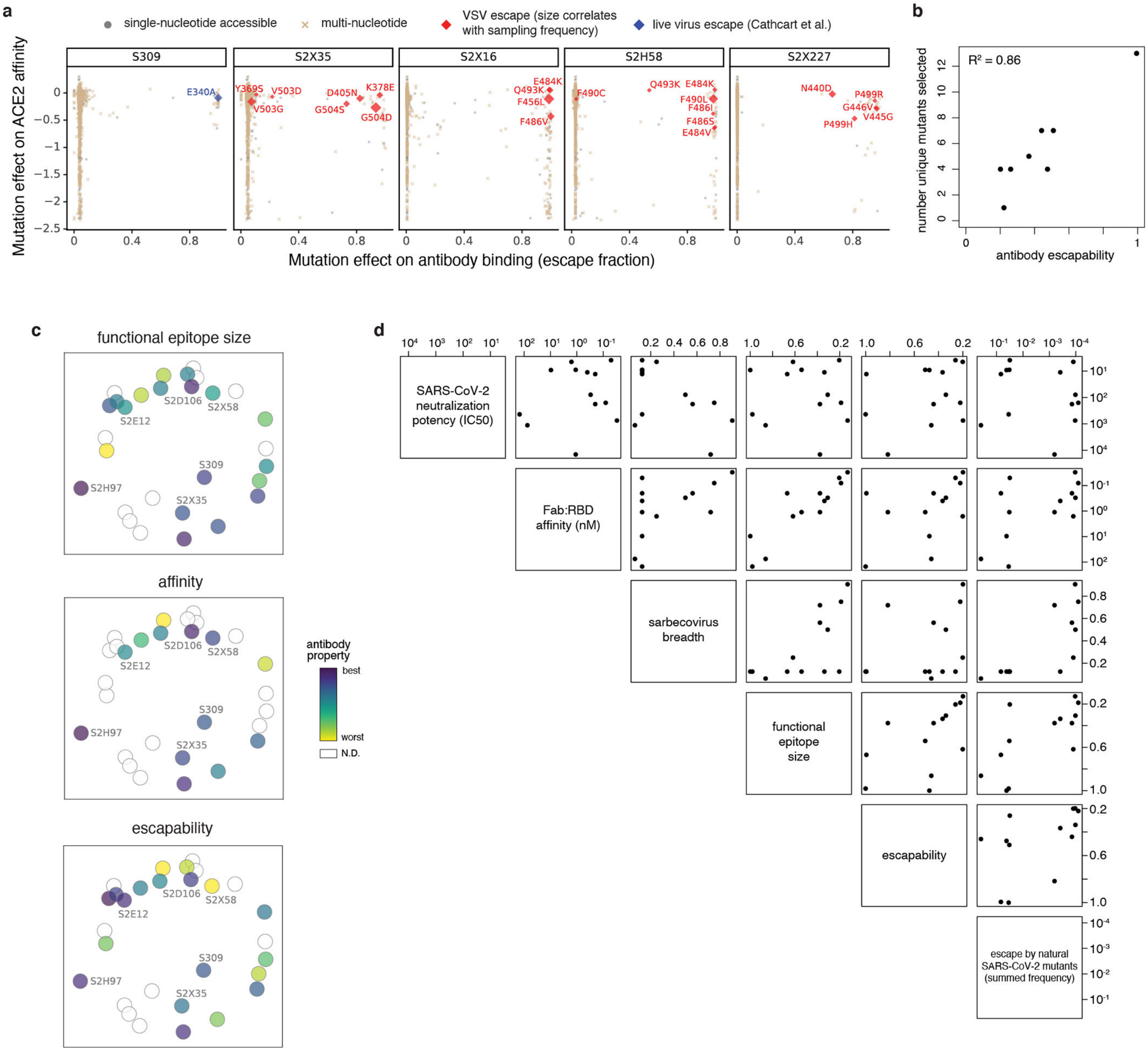

Extended Data Fig. 7. Escapability and the relationships among antibody properties.

a, Additional spike-VSV viral escape selections, as in Fig. 3a, and an illustration of the authentic SARS-CoV-2 escape data for S309 reported in Cathcart et al.[22]. **b**, Correlation between the number of unique mutations selected across viral escape selection experiments and antibody escapability as tabulated in Fig. 1b,c, plus S2X259[37]. **c**, Projected epitope space from Fig. 4a annotated by antibody properties as in Fig. 4b–d. For each property, antibodies are colored such that purple reflects the most desirable antibody (scale bar, right; N.D., not determined): narrowest functional epitope, tightest binding affinity (K_D, log10 scale), lowest escapability. **d**, Pairwise scatterplots between all antibody properties discussed in the main text. Select scatterplots from this panel are shown in Figs. 4e–g. Details of each property described in Methods. All axes are oriented such that moving up on the y-axis and right on the x-axis corresponds to moving in the "preferred" direction for an antibody property (lower neutralization IC50, lower K_D, higher breadth, narrower epitope size, lower escapability, lower total frequency of SARS-CoV-2 escape mutants among sequences on GISAID).

Extended Data Table 1.

Characteristics of the antibodies described in this study.

Mab ID	Site	Cross-reactive	ACE2 blocker	VH	HCDR3 length (amino acids)	VH identity to GL	VK/VL	IC50 (ng/mL)	IC90 (ng/mL)	IC50 (ng/mL)	IC90 (ng/mL)	Spike Apparent Affinity[§] by SPR (nM)	RBD Affinity by SPR (nM) (RBD ligand:Fab analyte; IgG ligand:RBD analyte)		S1 shedding	Effector function	RBD open vs closed	Days from symptoms onset	Somatic Hyper Mut. HC/LC
								VSV-pp		IF/luc		Fab	Fab	IgG					
S2E12	Ia	No	Yes	VH1-58	16	97.2%	VK3-20	2.0 (0.9–3.4)	12.4	4.5 (3–6)	14.0	2.5[†]	1.7 (1.61–1.76)	0.7	Yes	No	open	51	6/4
S2X58	Ib	No	Yes	VH1-46	12	99.0%	VK1-33	4.3 (2.7–8.8)	69.0	13.1 (7–20)	49.1	0.6	0.2 (0.20–0.24)	0.2	Yes	No	open	48	3/3
S2H58	Ib	No	Yes	VH1-2	15	97.9%	VK2-28	6.1 (1.7–15.7)	123.0	9.0 (6–11)	28.7	4.8	1.0 (0.99–1.08)	1.5	No	Yes	NA	45	6/3
S2D106	Ia	No	Yes	VH1-69	19	97.2%	VK1-39	4.3 (3.5–6.5)	25.6	6.8 (5–9)	23.6	0.17	0.05 (0.046–0.049)	0.04	Yes	No	open	98	5/3
S2X227	Ib	No	Yes	VH1-46	14	97.9%	VK4-1	5.3 (4.4–6.2)	26.9	11.2 (9–13)	36.0	0.11	0.4 (0.41–0.46)	0.1	No	Yes	NA	75	3/2
S2X16	Ia	No	Yes	VH1-69	18	97.6%	VK2-28	8.1 (2.6–14.9)	62.1	9.2 (4–16)	39.7	11.1	9.2 (8.83–9.59)	6.1[‖]	Yes	No	NA	48	3/2
S304	IIc	Yes	No	VH3-13	14	98.6%	VK1-39	9405 (8827–9795)	n/a	14412 (7573–29889)	n/a	8.7[*]	1.0 (0.93–1.17)	0.4	Yes	No	open	10y	5/6
S309	IV	Yes	No	VH1-18	20	97.2%	VK3-20	31.1 (23.0–58.7)	160.9	78.9 (52–121)	300.3	~0.2[*]	0.2 (0.17–0.31)	0.2[‡]	No	Yes	open/ closed	10y	8/6
S2X35	IIa	Yes	Yes	VH1-18	21	98.6%	VL1-40	96.2 (67.8–144.9)	530.5	179.4 (121–219)	592.5	~0.1[*]	0.2 (0.18–0.22)	0.06	Yes	No	open	48	4/1
S2H97	V	Yes	No	VH5-51	13	98.3%	VL2-14	337.6 (277–406)	3656.1	748.7 (540–1120)	3290.7	~2	0.04 (0.031–0.060)	0.04	Yes	No	open	81	7/6
S2H13	Ib	No	Yes	VH3-7	13	97.9%	VL7-46	637.6 (494–856)	6745.9	435.3 (331–656)	1390.1	119[*]	123 (108–149)	33[‖]	No	Yes	open/ closed	17	4/1
S2H14	Ia	No	Yes	VH3-15	17	100.0%	VL6-57	1274.0 (1027–1436)	8735.3	1130.3 (522–2583)	5121.8	90.1[*]	71 (56–77)	65[‖]	Yes	No	open	17	0/0

VH and VL percent identity refers to V gene segment identity compared to germline (as per the International Immunogenetics Information System (http://www.imgt.org/)). HCDR3 length was determined using IMGT. SARS-CoV-2 neutralization potency (authentic virus [*n*=3] and spike-pseudotyped VSV particles [*n* = 3 to 8] on Vero E6 cells), Fab:RBD binding affinities measured by SPR [*n* = 2 to 4]. Some binding affinities for previously described antibodies were measured in Piccoli et al. (S304, S309, S2X35, S2H13, S2H14)

[*] Tortorici et al. (S2E12)

[†] Cathcart et al. (S309)

[‡] Values in brackets are minimum and maximum determined values.

[§] Spike binding data are “apparent affinity” or $K_{D,app}$, because RBD conformational dynamics affect the kinetics. S2H97 Fab binding to spike doesn’t fit well to 1:1 binding, presumably because of changing epitope accessibility.

[//] Biphasic kinetics; Fit result is for fast phase

Extended Data Table 2.

Crystallographic data collection and refinement statistics.

	RBD/S2X35/S309 PDB 7R6W	RBD/S2H97/S2X259 PDB 7M7W	RBD/S2E12/S309/S304 PDB 7R6X
Data collection			
Space group	C222	$P2_1$	$I4_122$
Cell dimensions			
a, b, c (Å)	106.27, 239.37, 129.81	86.19, 66.40, 237.66	245.87, 245.87, 237.31
α, β, γ (°)	90.00, 90.00, 90.00	90.00, 94.34, 90.00	90.00, 90.00, 90.00
Resolution (Å)	39.52–1.83 (1.86–1.83)	63.94–2.65 (2.70–2.65)	49.00–2.93 (2.99–2.93)
R_{merge}	0.085 (2.96)	0.149/2.494	0.295/7.868
$I / \sigma I$	16.2 (0.7)	10.9 (0.8)	13.3 (0.5)
Completeness (%)	99.6 (99.5)	98.6 (98.3)	100.00 (100.00)
Redundancy	6.7 (7.0)	6.9 (6.8)	28.9 (27.2)
Refinement			
Resolution (Å)	1.83	2.65	2.95
No. reflections	135,667	73,189	71,532
$R_{\text{work}} / R_{\text{free}}$	0.211/0.232	0.221/0.271	0.232/0.262
No. atoms			
Protein	8160	16,162	9,101
Ligand/ion	172	28	16
Water	584	95	3
B-factors			
Protein	39.56	75.86	116.53
Ligand/ion	75.00	84.00	122.00
Water	42.94	50.09	65.90
R.m.s. deviations			
Bond lengths (Å)	0.004	0.002	0.003
Bond angles (°)	1.259	0.817	0.936

Extended Data Table 3.

CryoEM data collection, refinement, and validation statistics.

	SARS-CoV-2 S/S2D106 (EMD-24300)	SARS-CoV-2 S/S2D106 (local refinement) (EMD-24299) (PDB 7R7N)	SARS-CoV-2 S/S2H97 (EMD-24301)
Data collection and processing			
Magnification	130,000	130,000	36,000
Voltage (kV)	300	300	200
Electron exposure (e–/Å^2)	70	70	60

	SARS-CoV-2 S/S2D106 (EMD-24300)	**SARS-CoV-2 S/S2D106 (local refinement) (EMD-24299) (PDB 7R7N)**	**SARS-CoV-2 S/S2H97 (EMD-24301)**
Defocus range (μm)	−0.5 – −2.5	−0.5 – −2.5	−0.5 – −3.0
Pixel size (Å)	0.525	0.525	1.16
Symmetry imposed	C1	C1	C1
Initial particle images (no.)	175,479	87,587	98,950
Map resolution (Å)	3.7	4.0	3.6
FSC threshold	0.143	0.143	0.143
Map sharpening *B* factor ($Å^2$)	−61	−17	−70
Validation			
MolProbity score		0.89	
Clashscore		0.58	
Poor rotamers (%)		0.45	
Ramachandran plot			
Favored (%)		96.78	
Allowed (%)		3.22	
Disallowed (%)		0	

Authors

Tyler N. Starr[1,*], Nadine Czudnochowski[2,*], Zhuoming Liu[3,*], Fabrizia Zatta[4], Young-Jun Park[5], Amin Addetia[1], Dora Pinto[4], Martina Beltramello[4], Patrick Hernandez[2], Allison J. Greaney[1,6], Roberta Marzi[4], William G. Glass[7], Ivy Zhang[7,8], Adam S. Dingens[1], John E. Bowen[5], M. Alejandra Tortorici[5], Alexandra C. Walls[5], Jason A. Wojcechowskyj[2], Anna De Marco[4], Laura E. Rosen[2], Jiayi Zhou[2], Martin Montiel-Ruiz[2], Hannah Kaiser[2], Josh Dillen[2], Heather Tucker[2], Jessica Bassi[4], Chiara Silacci-Fregni[4], Michael P. Housley[2], Julia di Iulio[2], Gloria Lombardo[4], Maria Agostini[2], Nicole Sprugasci[4], Katja Culap[4], Stefano Jaconi[4], Marcel Meury[2], Exequiel Dellota[2], Rana Abdelnabi[9], Shi-Yan Caroline Foo[9], Elisabetta Cameroni[4], Spencer Stumpf[3], Tristan I. Croll[10], Jay C. Nix[11], Colin Havenar-Daughton[2], Luca Piccoli[4], Fabio Benigni[4], Johan Neyts[9], Amalio Telenti[2], Florian A. Lempp[2], Matteo S. Pizzuto[4], John D. Chodera[7], Christy M. Hebner[2], Herbert W. Virgin[2,12,13], Sean P.J. Whelan[3], David Veesler[5], Davide Corti[4,†], Jesse D. Bloom[1,6,14,†], Gyorgy Snell[2,†]

Affiliations

[1]Basic Sciences Division, Fred Hutchinson Cancer Research Center, Seattle, WA 98109, USA

[2]Vir Biotechnology, San Francisco, CA 94158, USA

[3]Department of Molecular Microbiology, Washington University School of Medicine, St. Louis, MO 63110, USA

[4]Humabs BioMed SA, a subsidiary of Vir Biotechnology, 6500 Bellinzona, Switzerland

[5]Department of Biochemistry, University of Washington, Seattle, WA 98195, USA

[6]Department of Genome Sciences, University of Washington, Seattle, WA 98195, USA

[7]Computational and Systems Biology Program, Sloan Kettering Institute, Memorial Sloan Kettering Cancer Center, New York, NY 10065, USA

[8]Tri-Institutional PhD Program in Computational Biology and Medicine, Weill Cornell Graduate School of Medical Sciences, New York, NY 10065, USA

[9]Rega Institute for Medical Research, Laboratory of Virology and Chemotherapy, KU Leuven, Belgium

[10]Cambridge Institute for Medical Research, Department of Haematology, University of Cambridge, Cambridge, CB2 0XY, UK

[11]Molecular Biology Consortium, Advanced Light Source, Lawrence Berkeley National Laboratory, Berkeley, CA 94720, USA

[12]Department of Pathology and Immunology, Washington University School of Medicine, Saint Louis, MO 63110, USA

[13]Department of Internal Medicine, UT Southwestern Medical Center, Dallas, TX 75390, USA

[14]Howard Hughes Medical Institute, Seattle, WA 98109, USA

ACKNOWLEDGEMENTS

We thank Isaac Hoffman for assistance in refinement of crystal structures, Gregory R. Bowman, Joseph Coffland, and Peter K. Eastman for developing and maintaining the Folding@home infrastructure, Amazon Web Services for Folding@home infrastructure support, the Folding@home volunteers who contributed their computational resources to this project (FAH Project 17336-17340), Rafal P. Wiewiora and Sukrit Singh for their assistance with Folding@home, and Aoife M. Harbison and Elisa Fadda for assistance in glycan modeling. This work was supported by the Fred Hutch Flow Cytometry and Genomics facilities, the Fred Hutch Scientific Computing group supported by ORIP grant S10OD028685, and the University of Washington Arnold and Mabel Beckman cryoEM center. This work was supported by the NIH/NIAID (R01AI127893 and R01AI141707 to JDB, DP1AI158186 and HHSN272201700059C to DV, T32AI083203 to AJG), the NIH/NIGMS (R01GM120553 to DV, and grant R01GM121505 and R01GM132386 to JDC), the NIH/NCI (P30CA008748 to JDC), the National Science Foundation (NSF CHI-1904822 to JDC), the Damon Runyon Cancer Research Foundation (TNS), the Gates Foundation (INV-004949 to JDB), a Pew Biomedical Scholars Award (DV), Investigators in the Pathogenesis of Infectious Disease Awards from the Burroughs Wellcome Fund (JDB and DV), the Wellcome Trust (209407/Z/17/Z to TIC), Fast Grants (DV), Bayer (WGG) and the Molecular Sciences Software Institute (IZ). JDB is an Investigator of the Howard Hughes Medical Institute. The Molecular Biology Consortium beamline 4.2.2 of the Advanced Light Source, a U.S. DOE Office of Science User Facility under Contract No. DE-AC02-05CH11231, is supported in part by the ALS-ENABLE program funded by the NIH/NIGMS (P30GM124169-01). Use of the Stanford Synchrotron Radiation Lightsource, SLAC National Accelerator Laboratory, is supported by the U.S. Department of Energy, Office of Science, Office of Basic Energy Sciences under Contract No. DE-AC02-76SF00515. The SSRL Structural Molecular Biology Program is supported by the DOE Office of Biological and Environmental Research, and by the NIH/NIGMS (P30GM133894).

REFERENCES

1. Liu Z et al. Identification of SARS-CoV-2 spike mutations that attenuate monoclonal and serum antibody neutralization. Cell Host Microbe 29, 477–488.e4 (2021). [PubMed: 33535027]

2. Weisblum Y et al. Escape from neutralizing antibodies by SARS-CoV-2 spike protein variants. Elife 9, e61312 (2020). [PubMed: 33112236]
3. Greaney AJ et al. Complete Mapping of Mutations to the SARS-CoV-2 Spike Receptor-Binding Domain that Escape Antibody Recognition. Cell Host Microbe 29, 44–57.e9 (2021). [PubMed: 33259788]
4. Pinto D et al. Cross-neutralization of SARS-CoV-2 by a human monoclonal SARS-CoV antibody. Nature 583, 290–295 (2020). [PubMed: 32422645]
5. Rappazzo CG et al. Broad and potent activity against SARS-like viruses by an engineered human monoclonal antibody. Science 371, 823–829 (2021). [PubMed: 33495307]
6. Menachery VD et al. A SARS-like cluster of circulating bat coronaviruses shows potential for human emergence. Nat. Med. 21, 1508–1513 (2015). [PubMed: 26552008]
7. Letko M, Marzi A & Munster V Functional assessment of cell entry and receptor usage for SARS-CoV-2 and other lineage B betacoronaviruses. Nat Microbiol 5, 562–569 (2020). [PubMed: 32094589]
8. Tortorici MA et al. Ultrapotent human antibodies protect against SARS-CoV-2 challenge via multiple mechanisms. Science 370, 950–957 (2020). [PubMed: 32972994]
9. Barnes CO et al. SARS-CoV-2 neutralizing antibody structures inform therapeutic strategies. Nature 588, 682–687 (2020). [PubMed: 33045718]
10. Zost SJ et al. Potently neutralizing and protective human antibodies against SARS-CoV-2. Nature 584, 443–449 (2020). [PubMed: 32668443]
11. Hassan AO et al. A SARS-CoV-2 Infection Model in Mice Demonstrates Protection by Neutralizing Antibodies. Cell 182, 744–753.e4 (2020). [PubMed: 32553273]
12. Winkler ES et al. Human neutralizing antibodies against SARS-CoV-2 require intact Fc effector functions for optimal therapeutic protection. Cell 184, 1804–1820.e16 (2021). [PubMed: 33691139]
13. Schäfer A et al. Antibody potency, effector function, and combinations in protection and therapy for SARS-CoV-2 infection in vivo. J. Exp. Med. 218, (2021).
14. Corti D, Purcell LA, Snell G & Veesler D Tackling COVID-19 with neutralizing monoclonal antibodies. Cell 184, (2021).
15. Piccoli L et al. Mapping Neutralizing and Immunodominant Sites on the SARS-CoV-2 Spike Receptor-Binding Domain by Structure-Guided High-Resolution Serology. Cell 183, 1024–1042.e21 (2020). [PubMed: 32991844]
16. Greaney AJ et al. Comprehensive mapping of mutations in the SARS-CoV-2 receptor-binding domain that affect recognition by polyclonal human plasma antibodies. Cell Host Microbe 29, 463–476.e6 (2021). [PubMed: 33592168]
17. Chen RE et al. Resistance of SARS-CoV-2 variants to neutralization by monoclonal and serum-derived polyclonal antibodies. Nat. Med. 27, 717–726 (2021). [PubMed: 33664494]
18. Wang P et al. Antibody resistance of SARS-CoV-2 variants B.1.351 and B.1.1.7. Nature 593, 130–135 (2021). [PubMed: 33684923]
19. Thomson EC et al. Circulating SARS-CoV-2 spike N439K variants maintain fitness while evading antibody-mediated immunity. Cell 184, 1171–1187.e20 (2021). [PubMed: 33621484]
20. Starr TN et al. Prospective mapping of viral mutations that escape antibodies used to treat COVID-19. Science 371, 850–854 (2021). [PubMed: 33495308]
21. Starr TN, Greaney AJ, Dingens AS & Bloom JD Complete map of SARS-CoV-2 RBD mutations that escape the monoclonal antibody LY-CoV555 and its cocktail with LY-CoV016. Cell Rep Med 2, 100255 (2021). [PubMed: 33842902]
22. Cathcart AL et al. The dual function monoclonal antibodies VIR-7831 and VIR-7832 demonstrate potent in vitro and in vivo activity against SARS-CoV-2. bioRxiv 2021.03.09.434607 (2021) doi:10.1101/2021.03.09.434607.
23. McCallum M et al. SARS-CoV-2 immune evasion by variant B.1.427/B.1.429. bioRxiv (2021) doi:10.1101/2021.03.31.437925.
24. Gupta A et al. Early Covid-19 treatment with SARS-CoV-2 neutralizing antibody sotrovimab. medRxiv (2021) doi:10.1101/2021.05.27.21257096.

25. Dingens AS, Arenz D, Weight H, Overbaugh J & Bloom JD An Antigenic Atlas of HIV-1 Escape from Broadly Neutralizing Antibodies Distinguishes Functional and Structural Epitopes. Immunity 50, 520–532.e3 (2019). [PubMed: 30709739]
26. Starr TN et al. Deep Mutational Scanning of SARS-CoV-2 Receptor Binding Domain Reveals Constraints on Folding and ACE2 Binding. Cell 182, 1295–1310.e20 (2020). [PubMed: 32841599]
27. Faria NR et al. Genomics and epidemiology of a novel SARS-CoV-2 lineage in Manaus, Brazil. medRxiv 2021.02.26.21252554 (2021).
28. Tegally H et al. Detection of a SARS-CoV-2 variant of concern in South Africa. Nature 592, 438–443 (2021). [PubMed: 33690265]
29. Zhang W et al. Emergence of a Novel SARS-CoV-2 Variant in Southern California. JAMA (2021) doi:10.1001/jama.2021.1612.
30. Walls AC et al. Unexpected Receptor Functional Mimicry Elucidates Activation of Coronavirus Fusion. Cell 176, 1026–1039.e15 (2019). [PubMed: 30712865]
31. Lempp FA et al. Membrane lectins enhance SARS-CoV-2 infection and influence the neutralizing activity of different classes of antibodies. bioRxiv 2021.04.03.438258 (2021) doi:10.1101/2021.04.03.438258.
32. Pinto D et al. A human antibody that broadly neutralizes betacoronaviruses protects against SARS-CoV-2 by blocking the fusion machinery. bioRxiv 2021.05.09.442808 (2021) doi:10.1101/2021.05.09.442808.
33. Walls AC et al. Elicitation of Potent Neutralizing Antibody Responses by Designed Protein Nanoparticle Vaccines for SARS-CoV-2. Cell 183, 1367–1382.e17 (2020). [PubMed: 33160446]
34. Cohen AA et al. Mosaic nanoparticles elicit cross-reactive immune responses to zoonotic coronaviruses in mice. Science 371, 735–741 (2021). [PubMed: 33436524]
35. Saunders KO et al. Neutralizing antibody vaccine for pandemic and pre-emergent coronaviruses. Nature (2021) doi:10.1038/s41586-021-03594-0.
36. Dong J et al. Genetic and structural basis for recognition of SARS-CoV-2 spike protein by a two-antibody cocktail. bioRxiv 2021.01.27.428529 (2021) doi:10.1101/2021.01.27.428529.
37. Tortorici MA et al. Structural basis for broad sarbecovirus neutralization by a human monoclonal antibody. bioRxiv 2021.04.07.438818 (2021) doi:10.1101/2021.04.07.438818.
38. Sauer MM et al. Structural basis for broad coronavirus neutralization. Nat. Struct. Mol. Biol. (2021) doi:10.1038/s41594-021-00596-4.
39. Kistler KE & Bedford T Evidence for adaptive evolution in the receptor-binding domain of seasonal coronaviruses OC43 and 229e. Elife 10, (2021).
40. Eguia RT et al. A human coronavirus evolves antigenically to escape antibody immunity. PLoS Pathog. 17, e1009453 (2021). [PubMed: 33831132]
41. Walls AC et al. Elicitation of broadly protective sarbecovirus immunity by receptor-binding domain nanoparticle vaccines. bioRxiv 2021.03.15.435528 (2021) doi:10.1101/2021.03.15.435528.
42. Zhou P et al. A protective broadly cross-reactive human antibody defines a conserved site of vulnerability on beta-coronavirus spikes. bioRxiv 2021.03.30.437769 (2021) doi:10.1101/2021.03.30.437769.
43. Crawford KHD et al. Protocol and Reagents for Pseudotyping Lentiviral Particles with SARS-CoV-2 Spike Protein for Neutralization Assays. Viruses 12, (2020).
44. Xie X et al. A nanoluciferase SARS-CoV-2 for rapid neutralization testing and screening of anti-infective drugs for COVID-19. Nat. Commun. 11, 5214 (2020). [PubMed: 33060595]
45. Takada A et al. A system for functional analysis of Ebola virus glycoprotein. Proc. Natl. Acad. Sci. U. S. A. 94, 14764–14769 (1997). [PubMed: 9405687]
46. Riblett AM et al. A Haploid Genetic Screen Identifies Heparan Sulfate Proteoglycans Supporting Rift Valley Fever Virus Infection. J. Virol. 90, 1414–1423 (2016). [PubMed: 26581979]
47. Giroglou T et al. Retroviral vectors pseudotyped with severe acute respiratory syndrome coronavirus S protein. J. Virol. 78, 9007–9015 (2004). [PubMed: 15308697]
48. Collier DA et al. Sensitivity of SARS-CoV-2 B.1.1.7 to mRNA vaccine-elicited antibodies. Nature 593, 136–141 (2021). [PubMed: 33706364]

49. Walls AC et al. Structure, Function, and Antigenicity of the SARS-CoV-2 Spike Glycoprotein. Cell 181, 281–292.e6 (2020). [PubMed: 32155444]

50. Otwinowski J, McCandlish DM & Plotkin JB Inferring the shape of global epistasis. Proc. Natl. Acad. Sci. U. S. A. 115, E7550–E7558 (2018). [PubMed: 30037990]

51. Hilton S et al. dms-view: Interactive visualization tool for deep mutational scanning data. J. Open Source Softw. 5, 2353 (2020). [PubMed: 34189395]

52. Song H-D et al. Cross-host evolution of severe acute respiratory syndrome coronavirus in palm civet and human. Proc. Natl. Acad. Sci. U. S. A. 102, 2430–2435 (2005). [PubMed: 15695582]

53. Tong S et al. Detection of novel SARS-like and other coronaviruses in bats from Kenya. Emerg. Infect. Dis. 15, 482–485 (2009). [PubMed: 19239771]

54. Zhou H et al. A Novel Bat Coronavirus Closely Related to SARS-CoV-2 Contains Natural Insertions at the S1/S2 Cleavage Site of the Spike Protein. Curr. Biol. 30, 2196–2203.e3 (2020). [PubMed: 32416074]

55. Lam TT-Y et al. Identifying SARS-CoV-2-related coronaviruses in Malayan pangolins. Nature 583, 282–285 (2020). [PubMed: 32218527]

56. Katoh K & Standley DM MAFFT multiple sequence alignment software version 7: improvements in performance and usability. Mol. Biol. Evol. 30, 772–780 (2013). [PubMed: 23329690]

57. Suyama M, Torrents D & Bork P PAL2NAL: robust conversion of protein sequence alignments into the corresponding codon alignments. Nucleic Acids Res. 34, W609–12 (2006). [PubMed: 16845082]

58. Stamatakis A RAxML version 8: a tool for phylogenetic analysis and post-analysis of large phylogenies. Bioinformatics 30, 1312–1313 (2014). [PubMed: 24451623]

59. Elbe S & Buckland-Merrett G Data, disease and diplomacy: GISAID’s innovative contribution to global health. Glob Chall 1, 33–46 (2017). [PubMed: 31565258]

60. Lan J et al. Structure of the SARS-CoV-2 spike receptor-binding domain bound to the ACE2 receptor. Nature 581, 215–220 (2020). [PubMed: 32225176]

61. Yuan M et al. A highly conserved cryptic epitope in the receptor binding domains of SARS-CoV-2 and SARS-CoV. Science 368, 630–633 (2020). [PubMed: 32245784]

62. Hansen J et al. Studies in humanized mice and convalescent humans yield a SARS-CoV-2 antibody cocktail. Science 369, 1010–1014 (2020). [PubMed: 32540901]

63. Shi R et al. A human neutralizing antibody targets the receptor-binding site of SARS-CoV-2. Nature 584, 120–124 (2020). [PubMed: 32454512]

64. Kabsch W XDS. Acta Crystallogr. D Biol. Crystallogr. 66, 125–132 (2010). [PubMed: 20124692]

65. McCoy AJ et al. Phaser crystallographic software. J. Appl. Crystallogr. 40, 658–674 (2007). [PubMed: 19461840]

66. Emsley P, Lohkamp B, Scott WG & Cowtan K Features and development of coot. Acta Crystallogr. D Biol. Crystallogr. 66, 486–501 (2010). [PubMed: 20383002]

67. Croll TI ISOLDE: a physically realistic environment for model building into low-resolution electron-density maps. Acta Crystallogr. D Struct. Biol. 74, 519–530 (2018). [PubMed: 29872003]

68. Murshudov GN et al. REFMAC5 for the refinement of macromolecular crystal structures. Acta Crystallogr. D Biol. Crystallogr. 67, 355–367 (2011). [PubMed: 21460454]

69. Hsieh C-L et al. Structure-based design of prefusion-stabilized SARS-CoV-2 spikes. Science 369, 1501–1505 (2020). [PubMed: 32703906]

70. Suloway C et al. Automated molecular microscopy: the new Leginon system. J. Struct. Biol. 151, 41–60 (2005). [PubMed: 15890530]

71. Tegunov D & Cramer P Real-time cryo-electron microscopy data preprocessing with Warp. Nat. Methods 16, 1146–1152 (2019). [PubMed: 31591575]

72. Punjani A, Rubinstein JL, Fleet DJ & Brubaker MA cryoSPARC: algorithms for rapid unsupervised cryo-EM structure determination. Nat. Methods 14, 290–296 (2017). [PubMed: 28165473]

73. Zivanov J et al. New tools for automated high-resolution cryo-EM structure determination in RELION-3. Elife 7, (2018).

74. Punjani A, Zhang H & Fleet DJ Non-uniform refinement: adaptive regularization improves single-particle cryo-EM reconstruction. Nat. Methods 17, 1214–1221 (2020). [PubMed: 33257830]

75. Zivanov J, Nakane T & Scheres SHW A Bayesian approach to beam-induced motion correction in cryo-EM single-particle analysis. IUCrJ 6, 5–17 (2019).

76. Ramlaul K, Palmer CM, Nakane T & Aylett CHS Mitigating local over-fitting during single particle reconstruction with SIDESPLITTER. J. Struct. Biol. 211, 107545 (2020). [PubMed: 32534144]

77. Pettersen EF et al. UCSF ChimeraX: Structure visualization for researchers, educators, and developers. Protein Sci. 30, 70–82 (2021). [PubMed: 32881101]

78. Casañal A, Lohkamp B & Emsley P Current developments in Coot for macromolecular model building of Electron Cryo-microscopy and Crystallographic Data. Protein Sci. 29, 1069–1078 (2020). [PubMed: 31730249]

79. Wang RY-R et al. Automated structure refinement of macromolecular assemblies from cryo-EM maps using Rosetta. Elife 5, (2016).

80. McCallum M et al. N-terminal domain antigenic mapping reveals a site of vulnerability for SARS-CoV-2. Cell (2021) doi:10.1016/j.cell.2021.03.028.

81. Boudewijns R et al. STAT2 signaling restricts viral dissemination but drives severe pneumonia in SARS-CoV-2 infected hamsters. Nat. Commun. 11, 5838 (2020). [PubMed: 33203860]

82. Sanchez-Felipe L et al. A single-dose live-attenuated YF17D-vectored SARS-CoV-2 vaccine candidate. Nature 590, 320–325 (2021). [PubMed: 33260195]

83. Reed LJ & Muench H A simple method of estimating fifty percent endpoints. Am. J. Epidemiol. 27, 493–497 (1938).

84. Case JB et al. Neutralizing Antibody and Soluble ACE2 Inhibition of a Replication-Competent VSV-SARS-CoV-2 and a Clinical Isolate of SARS-CoV-2. Cell Host Microbe 28, 475–485.e5 (2020). [PubMed: 32735849]

85. Shajahan A et al. Comprehensive characterization of N- and O- glycosylation of SARS-CoV-2 human receptor angiotensin converting enzyme 2. Glycobiology (2020) doi:10.1093/glycob/cwaa101.

86. Watanabe Y, Allen JD, Wrapp D, McLellan JS & Crispin M Site-specific glycan analysis of the SARS-CoV-2 spike. Science 369, 330–333 (2020). [PubMed: 32366695]

87. Harbison AM, Brosnan LP, Fenlon K & Fadda E Sequence-to-structure dependence of isolated IgG Fc complex biantennary N-glycans: a molecular dynamics study. Glycobiology 29, 94–103 (2019). [PubMed: 30325416]

88. Case DA, Belfon K, Ben-Shalom IY, Brozell SR, Cerutti DS, Cheatham TE III, Cruzeiro VWD, Darden TA, Duke RE, Giambasu G, Gilson MK, Gohlke H, Goetz AW, Harris R, Izadi S, Izmailov SA, Kasavajhala K, Kovalenko A, Krasny R, Kurtzman T, Lee TS, LeGrand S, Li P, Lin C, Liu J, Luchko T, Luo R, Man V, Merz KM, Miao Y, Mikhailovskii O, Monard G, Nguyen H, Onufriev A, Pan F, Pantano S, Qi R, Roe DR, Roitberg A, Sagui C, Schott-Verdugo S, Shen J, Simmerling C, Skrynnikov NR, Smith J, Swails J, Walker RC, Wang J, Wilson L, Wolf RM, Wu X, Xiong Y, Xue Y, York DM and Kollman PA Amber 2020. (2020).

89. Maier JA et al. Ff14SB: Improving the accuracy of protein side chain and backbone parameters from ff99SB. J. Chem. Theory Comput. 11, 3696–3713 (2015). [PubMed: 26574453]

90. Kirschner KN et al. GLYCAM06: a generalizable biomolecular force field. Carbohydrates. J. Comput. Chem. 29, 622–655 (2008). [PubMed: 17849372]

91. Jorgensen WL, Chandrasekhar J, Madura JD, Impey RW & Klein ML Comparison of simple potential functions for simulating liquid water. J. Chem. Phys. 79, 926–935 (1983).

92. Li P, Song LF & Merz KM Jr. Systematic parameterization of monovalent ions employing the nonbonded model. J. Chem. Theory Comput. 11, 1645–1657 (2015). [PubMed: 26574374]

93. Leimkuhler B & Matthews C Robust and efficient configurational molecular sampling via Langevin dynamics. J. Chem. Phys. 138, 174102 (2013). [PubMed: 23656109]

94. Darden T, York D & Pedersen L Particle mesh Ewald: An N·log(N) method for Ewald sums in large systems. J. Chem. Phys. 98, 10089–10092 (1993).

95. Shirts M & Pande VS COMPUTING: Screen savers of the world unite! Science 290, 1903–1904 (2000). [PubMed: 17742054]

96. Zimmerman MI et al. Citizen scientists create an Exascale computer to combat COVID-19. bioRxivorg (2020) doi:10.1101/2020.06.27.175430.

97. McGibbon RT et al. MDTraj: A modern open library for the analysis of molecular dynamics trajectories. Biophys. J. 109, 1528–1532 (2015). [PubMed: 26488642]

98. Michaud-Agrawal N, Denning EJ, Woolf TB & Beckstein O MDAnalysis: a toolkit for the analysis of molecular dynamics simulations. J. Comput. Chem. 32, 2319–2327 (2011). [PubMed: 21500218]

99. Gowers R et al. MDAnalysis: A python package for the rapid analysis of molecular dynamics simulations. in Proceedings of the 15th Python in Science Conference (SciPy, 2016). doi:10.25080/majora-629e541a-00e.

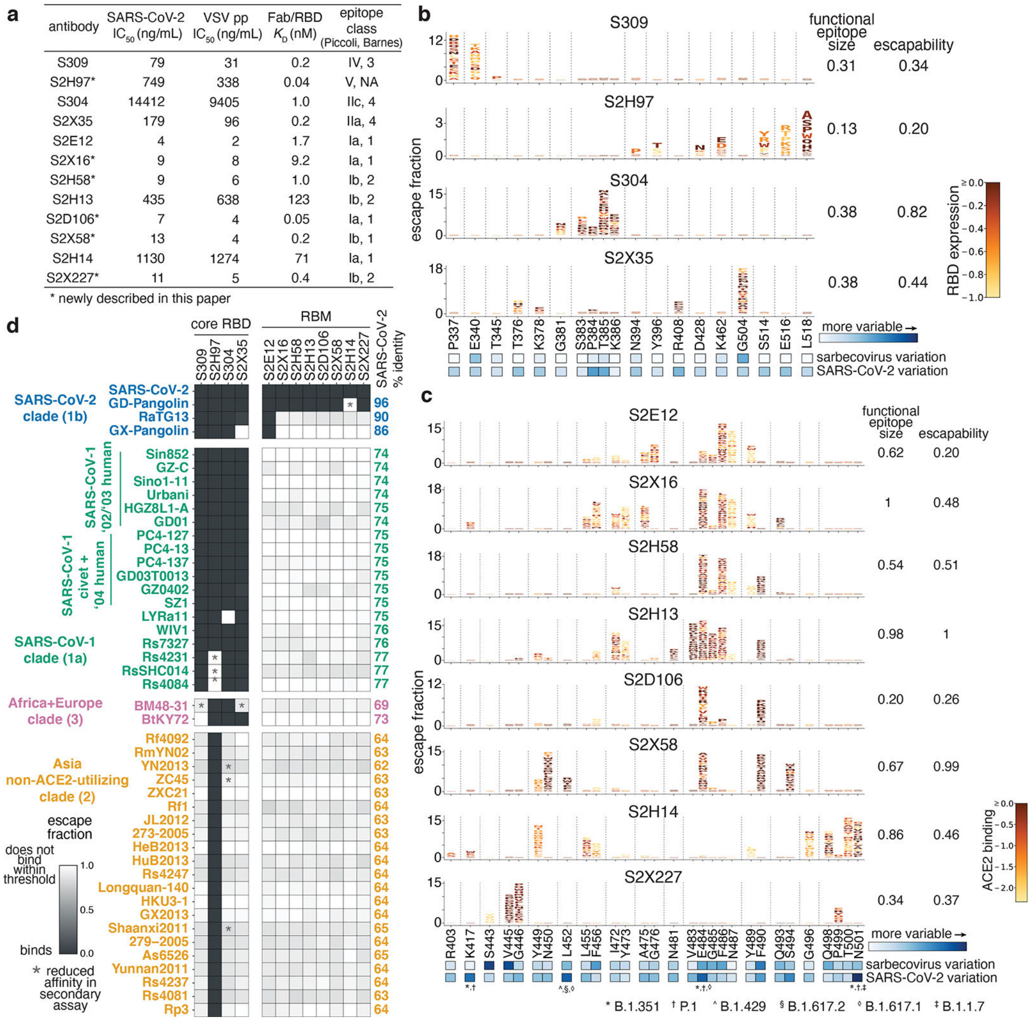

a

antibody	SARS-CoV-2 IC_{50} (ng/mL)	VSV pp IC_{50} (ng/mL)	Fab/RBD K_D (nM)	epitope class (Piccoli, Barnes)
S309	79	31	0.2	IV, 3
S2H97*	749	338	0.04	V, NA
S304	14412	9405	1.0	IIc, 4
S2X35	179	96	0.2	IIa, 4
S2E12	4	2	1.7	Ia, 1
S2X16*	9	8	9.2	Ia, 1
S2H58*	9	6	1.0	Ib, 2
S2H13	435	638	123	Ib, 2
S2D106*	7	4	0.05	Ia, 1
S2X58*	13	4	0.2	Ib, 1
S2H14	1130	1274	71	Ia, 1
S2X227*	11	5	0.4	Ib, 2

* newly described in this paper

Fig. 1. Potency, escapability, and breadth of a panel of RBD antibodies.

a, SARS-CoV-2 neutralization potency (authentic virus [*n*=3] and spike-pseudotyped VSV particles [*n* = 3 to 8] on Vero E6 cells), Fab:RBD binding affinities measured by SPR [*n* = 2 to 4], and epitope classifications. Additional details in Extended Data Table 1. **b,c**, Deep mutational scanning maps of mutations that escape binding by antibodies targeting the core RBD (**b**) or the receptor-binding motif (**c**). Letter height indicates that mutation's strength of escape from antibody binding. Letters colored by effect on folded RBD expression (**b**) or ACE2 binding affinity (**c**)[26]. Relative "functional epitope size" and "escapability" are tabulated at right, scaling from 0 (no escape mutations) to 1 (largest epitope/most escapable antibody). Heatmaps, bottom, illustrate variability among sarbecovirus or SARS-CoV-2 sequences. **d**, Antibody binding to a pan-sarbecovirus RBD panel. Heatmap illustrates binding from FACS-based selections (scale bar, bottom left). Asterisks, reduced-affinity binding in secondary binding assays (Extended Data Fig. 4a–f).

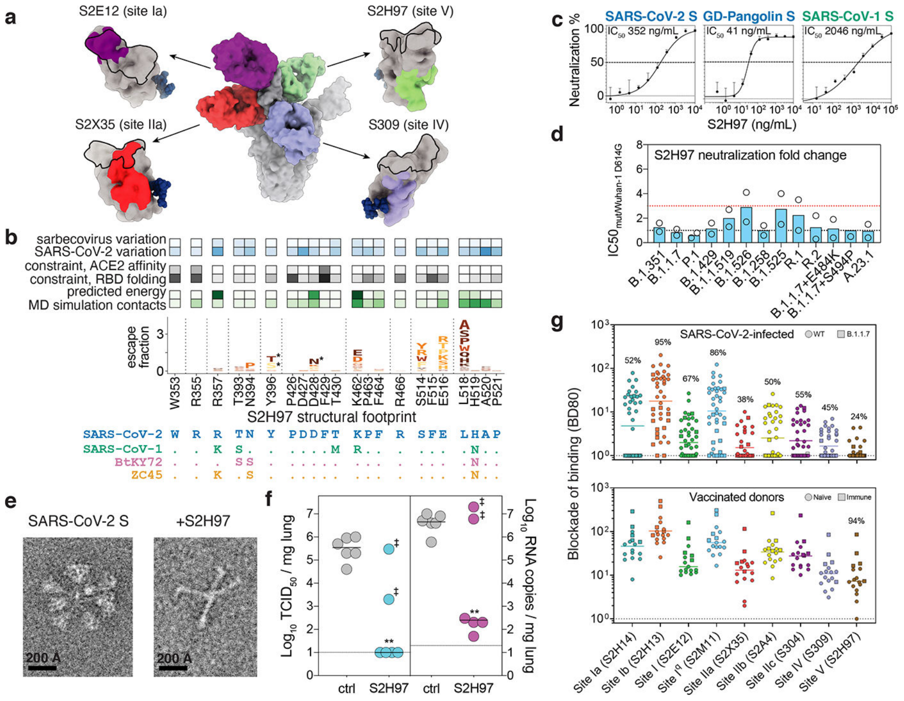

Fig. 2. The pan-sarbecovirus S2H97 antibody.

a, Composite model of the SARS-CoV-2 trimer with cross-reactive antibodies. Epitopes recognized by each Fab are shown as colored surface and ACE2 footprint as a black outline. **b**, Integrative features of the S2H97 structural footprint (5 Å cutoff). Heatmaps illustrate evolutionary variability (blue), functional constraint from prior deep mutational scans (gray), and energetic contribution to binding from the static crystal structure or molecular dynamics simulation (green). Logoplot as in Fig. 1b. Asterisk, introduction of N-linked glycosylation motifs. **c,** S2H97 breadth of neutralization (spike-pseudotyped VSV on Vero E6 cells). Curves representative of at least two independent experiments. Points represent means, error bars standard deviation from three technical replicates, and IC50 geometric mean of experiments. **d**, S2H97 neutralization of SARS-CoV-2 variants (Extended Data Fig. 1d; spike-pseudotyped VSV on Vero E6 cells). Points represent individual measurements and bar mean fold-change in neutralization potency. **e**, Negative stain EM imaging of native-like soluble prefusion S trimer (left) or S incubated with S2H97 (right). Micrographs representative of 51 (SARS-CoV-2 S) and 173 (+S2H97) micrographs. **f**, S2H97 prophylactic efficacy in Syrian hamsters. Infectious virus titers (left) and RNA levels (right) measured in hamsters four days after SARS-CoV-2 challenge in animals prophylactically dosed with 25 mg/kg S2H97 or isotype control. Two animals with undetectable S2H97 levels (<50 ng/mL) at the time of viral challenge are marked by ‡. ** p=0.0048 (virus titer) and p=0.0048 (RNA) vs control, two-sided Mann-Whitney test (animals with no detectable serum antibody excluded). **g**, Blockade of binding[15] by sera from SARS-CoV-2-infected (top) or vaccinated (bottom) donors. Percentage of samples with blockade above the lower detection limit are indicated.

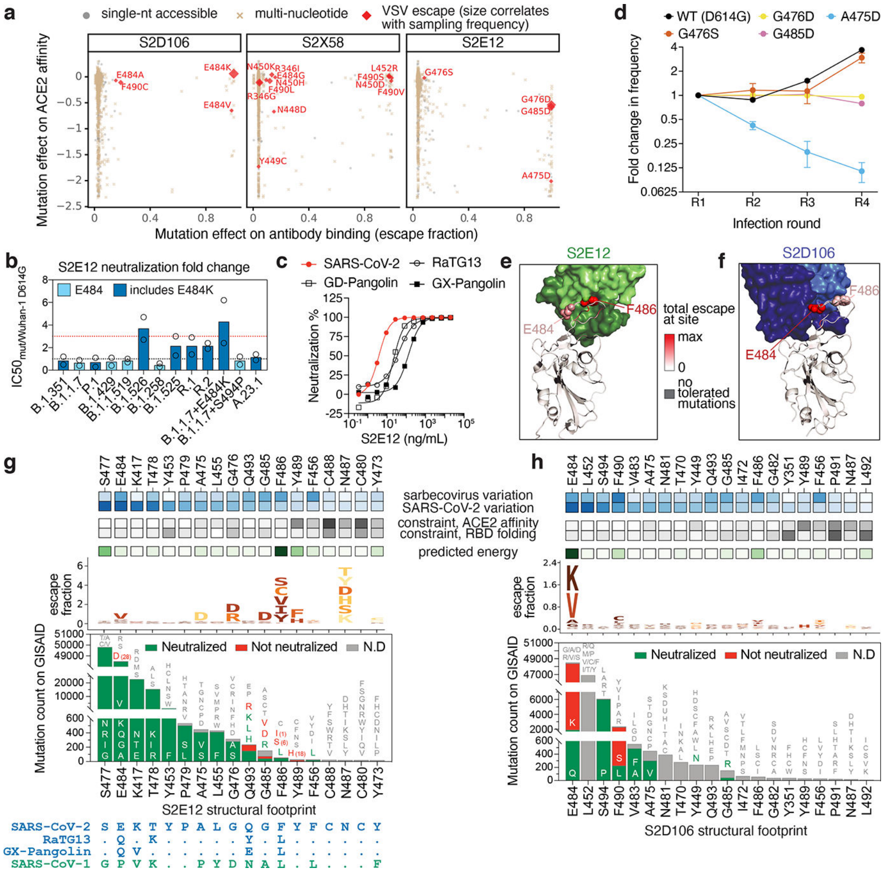

```
SARS-CoV-2   S E K T Y P A L G Q G F Y F C N C Y
RaTG13       . Q . K . . . . . . Y . L . . . . .
GX-Pangolin  . Q V . . . . . . . E . L . . . . .
SARS-CoV-1   G P V K . . P Y D N A L . L . . . F
```

Fig. 3. Breadth and escapability among RBM antibodies.

a, Escape mutations in spike-expressing VSV passaged in the presence of monoclonal antibody. Plot shows mutation effects on antibody (x-axis) and ACE2 (y-axis) binding. **b**, Neutralization of SARS-CoV-2 variants by S2E12 (spike-pseudotyped VSV on Vero E6 cells), as in Fig. 2d. **c**, S2E12 breadth of neutralization (spike-pseudotyped VSV on 293T-ACE2 cells). Points represent mean of biological duplicates. **d**, Replicative fitness of S2E12 escape mutations identified in (**a**) on Vero E6 cells. Points represent mean and error bars standard error from triplicate experiments. **e,f**, Structures of S2E12 Fab (**e**) and S2D106 Fab (**f**) bound to SARS-CoV-2 RBD. RBD sites colored by escape (scale bar, center). The E484 side chain is included for visualization purposes only but was not included in the final S2D106-bound structure due to weak density. **g,h**, Integrative features of the structural footprints (5 Å cutoff) of S2E12 (**g**) and S2D106 (**h**). Sites are ordered by the frequency of observed mutants among SARS-CoV-2 sequences on GISAID. Heatmaps as in Fig. 2b. Logoplots as in Fig. 1c, but only showing amino acid mutations accessible via single-nucleotide mutation from Wuhan-Hu-1 for comparison with (**a**). Barplots illustrate frequency of SARS-CoV-2 mutants and their validated effects on antibody neutralization (spike-pseudotyped VSV on Vero E6 cells). Red, >10-fold increase in IC50 due to mutation.

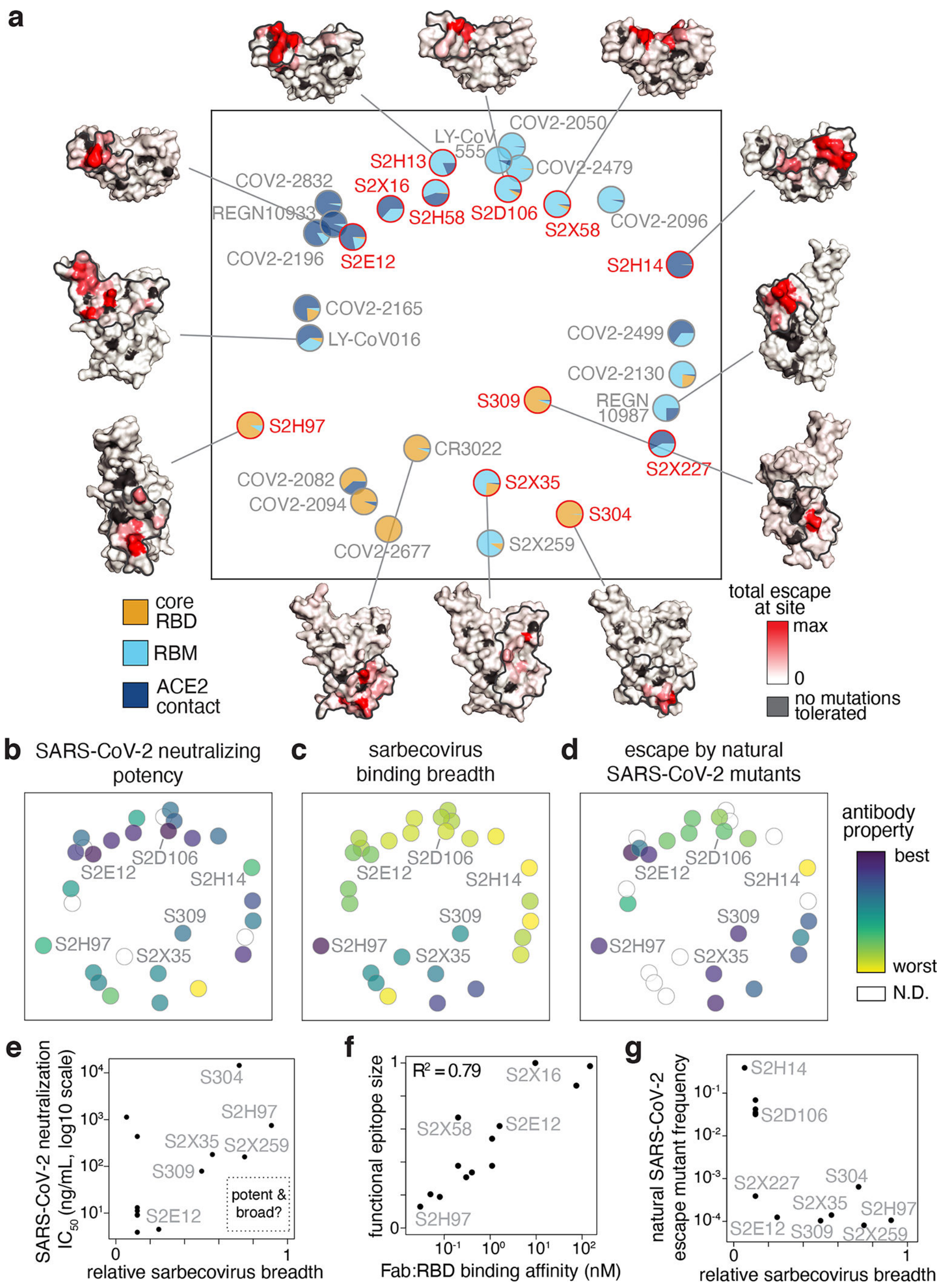

Fig. 4. Antibody epitope, potency, breadth, and escapability.

a, Multidimensional scaling projection of similarities in antibody binding-escape maps from this (red) and prior (gray) studies. Pie charts illustrate the RBD sub-domains where mutations confer escape (bottom left). Structural projections of escape arrayed around the perimeter (scale bar, bottom right), with gray outlines tracing structural footprints. **b-d**, Projected epitope space from (**a**) annotated by antibody properties. For each property, antibodies are colored such that purple reflects the most desirable antibody (scale bar, right): most potent neutralization (log10 scale), highest breadth, and lowest natural frequency of escape mutants (log10 scale). **e**, Relationship between SARS-CoV-2 neutralization potency and sarbecovirus breadth for antibodies in this study and S2X259[37]. **f**, Relationship between functional epitope size and SARS-CoV-2 RBD binding affinity. **g**, Relationship between natural SARS-CoV-2 escape mutant frequency (Extended Data Fig. 3c) and sarbecovirus breadth.